

# Hypernuclei formation in spallation reactions by coupling the Liège intranuclear cascade model to the deexcitation code ABLA

J. L. Rodríguez-Sánchez<sup>1,\*</sup>, J. Cugnon<sup>2</sup>, J.-C. David<sup>3</sup>, J. Hirtz<sup>3,4</sup>, A. Kelić-Heil<sup>5</sup>, and S. Leray<sup>3</sup>

<sup>1</sup>*IGFAE, Universidad de Santiago de Compostela, E-15782 Santiago de Compostela, Spain*

<sup>2</sup>*AGO Department, University of Liège, allée du 6 août 19, bâtiment B5, B-4000 Liège, Belgium*

<sup>3</sup>*IRFU, CEA, Université Paris-Saclay, F-91191 Gif-sur-Yvette, France*

<sup>4</sup>*Physics Institute, University of Bern, Sidlerstrasse 5, 3012 Bern, Switzerland*

<sup>5</sup>*GSI-Helmholtzzentrum für Schwerionenforschung GmbH, D-64291 Darmstadt, Germany*



(Received 29 October 2021; accepted 21 December 2021; published 24 January 2022)

Innovative experiments using the inverse kinematics technique to accelerate light, medium-mass, and heavy nuclei at relativistic energies have become excellent tools to produce and study hypernuclei. We investigate hypernuclei created in spallation reactions, where multifragmentation, particle evaporation, and fission processes play an important role in the formation of final hypernuclei residues. For the description of spallation reactions, we couple the Liège intranuclear cascade model, extended recently to the strange sector, to a new version of the ablation (ABLA) model that accounts for the evaporation of  $\Lambda$  particles from hot hyperremnants produced during the intranuclear cascade stage. These state of the art models are then used to study the production of hypernuclei close to drip lines through spallation-evaporation and fission reactions.

DOI: [10.1103/PhysRevC.105.014623](https://doi.org/10.1103/PhysRevC.105.014623)

## I. INTRODUCTION

Since the discovery in 1952 of the first hypernucleus in an experiment carried out with emulsion chambers [1], much effort has been invested in extending our knowledge of the nuclear chart toward the SU(3) flavor octets [2]. Hypernuclei are bound nuclear systems of strange baryons, the so-called hyperons, such as  $\Lambda$ ,  $\Sigma$ ,  $\Xi$ , or  $\Omega$ , produced in high-energy collisions. These hyperons can be captured by nuclei since their lifetimes are longer than the characteristic reaction times ( $\approx 10^{-23}$  s) [3]. Consequently, these studies on the production mechanism and structure of hypernuclei are of interest, because they provide information on the strange-matter properties and on the hyperon-nucleon ( $YN$ ) and hyperon-hyperon ( $YY$ ) interactions [4–10], which cannot be determined from scattering experiments.

Investigation of hypernuclear structure has important implications in the study of compact astrophysical objects. As shown in several works [11–15], the composition and equation of state (EOS) of supernovae and neutron star cores are poorly known due to their dependence on the hyperon content, with the hypernuclear weak decay being the only available tool to acquire knowledge on strangeness-changing weak baryon interactions. The understanding of the weak interactions, as well as of the strong ones, has a direct connection with astrophysics since they are important inputs when investigating the composition and macroscopic properties (masses and radii) of compact stars, their thermal evolution, and stability.

Among hypernuclei, the most known and long studied are  $\Lambda$  hypernuclei [16] in which a  $\Lambda$  particle, the lightest of the hyperons, replaces a nucleon of the nucleus.  $\Lambda$  hypernuclei are stable at the nuclear timescale ( $\approx 10^{-23}$  s) since the  $\Lambda$  particle maintains its identity even if embedded in a system of other nucleons, the only strong interaction allowed being  $\Lambda N$  scattering, which conserves strangeness. Similarly, two  $\Lambda$ 's may stick to a nuclear core, forming the so-called double  $\Lambda$  hypernuclei [17]. Moreover,  $\Xi$  hypernuclei also exist with binding energies similar to the ones obtained for  $\Lambda$  hypernuclei, although there are few measurements [18]. Other exotic systems like the  $\Omega$  hypernuclei are predicted by quark mean-field calculations [19], but so far no experimental data exist. On the other hand, the existing measurements for  $\Sigma$  hypernuclei indicate that these bound hypernuclei do not exist, at least as nuclear systems surviving for times longer than  $\approx 10^{-23}$  s due to its repulsive potential [20,21] and the strong  $\Sigma N \rightarrow \Lambda N$  conversion [22].

Many experimental collaborations, such as MPD and BM@N at the Nuclotron-based Ion Collider Facility (NICA) [23,24], STAR at the Relativistic Heavy Ion Collider (RHIC) [25,26], ALICE at the Large Hadron Collider (LHC) [27,28], PANDA [29,30], CBM [31], WASA@SuperFRS [32] and R<sup>3</sup>B [33,34] at the Facility for Antiproton and Ion Research (FAIR) [35], and HFRS at the High Intensity Heavy Ion Accelerator Facility (HIAF) [36,37], plan to produce light and medium-mass hypernuclei to investigate their properties in reactions induced by relativistic hadrons and ions. Here, spallation and fragmentation reactions are found to be the best tools to produce light, medium-mass, and heavy hypernuclei [26,38] to study interactions involving hyperons. The main purposes of these studies are, for example, the

\*Corresponding author: [joseluis.rodriguez.sanchez@usc.es](mailto:joseluis.rodriguez.sanchez@usc.es)

investigation of hypermatter structure, search for new constraints for the nuclear equation of state, and understand the possible phase transitions from hadronic matter to a quark-gluon plasma and the modification of hadron properties in dense strong-interacting matter [39,40]. In this work, we pay attention to the formation of hypernuclei in spallation reactions in which a light projectile, mainly a proton, neutron, or light nucleus, with the kinetic energy of a few of GeVs interacts with a heavy nucleus (e.g., uranium) and causes the emission of a large number of hadrons and/or some fragments. Spallation reactions are usually described by using hybrid models consisting of an intranuclear cascade (INC) stage followed by a statistical or dynamical deexcitation stage [41–44]. The timescale for the second stage is typically much longer than that for the first one, which justifies the fact that deexcitation is not described by INC models but by a different class of models which rely on statistical assumptions about the properties of the excited remnants.

On the one hand, the Liège intranuclear-cascade model (INCL) has been recently extended toward high energies ( $\approx 20$  GeV) including new interaction processes such as multipion production [45,46], production of  $\eta$  and  $\omega$  mesons [47], and strange particles like kaons and hyperons [48–50]. This new version of INCL permits us to predict the formation of hot hyperremnants and their characterization in atomic ( $Z$ ) and mass ( $A$ ) numbers, strangeness number ( $I_s$ ), excitation energy, and angular momenta. These improvements in the intranuclear cascade model require deexcitation models considering the emission of hyperons. Currently only a few deexcitation models treat the evaporation of hyperons and the formation of cold hypernuclei. The most known model is the statistical multifragmentation model (SMM) developed by Botvina and collaborators [51]; however, this model underestimates the production of normal evaporation residues and fission fragments coming from the deexcitation of heavy remnants [52,53] and, therefore, one could also expect an underestimation of cold hypernuclei produced in the deexcitation of heavy hyperremnants.

On the other hand, new state of the art experiments require the development of advanced simulations based on GEANT4 [54] where event generators must be written in C++. In this sense, a great effort has been performed by Mancusi and collaborators to rewrite the FORTRAN version of INCL in C++ and to implement it in GEANT4; however, deexcitation models did not follow this way. The most widely used deexcitation models are Gemini++ [44,55], SMM [51,56], and ABLA07 [57]. Gemini++ is written in C++, but the Hauser-Feshbach evaporation formalism used to calculate the particle emission probabilities increases the computing time too much and cannot be used in GEANT4 simulations. SMM and ABLA07 are faster than Gemini++, but they are written in FORTRAN and cannot be used directly in GEANT4. Recently, different benchmarks performed by the International Atomic Energy Agency (IAEA) [53,58] demonstrated that the best model to describe the deexcitation of hot remnants is ABLA07. For this reason, we decided to rewrite the FORTRAN version of ABLA07 in C++. This work was also utilized to introduce the emission of hyperons and the formation of cold hypernuclei.

This paper is devoted to the formation of cold hypernuclei produced in spallation reactions. In Sec. II, we describe briefly INCL and its new ingredients to produce hot hyperremnants. Then we make a general description of ABLA07 and explain the new ingredients introduced for modeling the emission of hyperons and the formation of cold hypernuclei. Finally, in Sec. III, we compare the new version of ABLA model to SMM calculations and also show the findings for cold hypernuclei production after particle evaporation, multifragmentation, and fission decay processes.

## II. MODEL DESCRIPTION

Spallation reactions at relativistic energies are often described by means of a two-step process [41]: the collision itself, where part of the nucleons are removed from target nuclei and some excitation energy and angular momenta are gained by the remnants, and subsequent de-excitation processes by evaporation of particles or fission. If the temperature of the hot remnants produced after the collision is high enough, the remnants could break up into lighter fragments, resulting in the so-called multifragmentation process. In the following, we will describe the models and all these decay mechanisms.

### A. Liège intranuclear-cascade code

The collision between projectile (baryons, light particles, or ions) and target (nuclei) is described by intranuclear cascade models; see, for instance, Refs. [59–65] and references therein. In this context, it is assumed that the reaction can be described as an avalanche of independent binary collisions. The INCL model is essentially classical, with the addition of a few suitable ingredients that mimic genuine quantum-mechanical features of the initial conditions and of the dynamics: For instance, target nucleons are endowed with Fermi motion, realistic space densities are used, the output of binary collisions is randomized and elementary baryon-baryon collisions are subject to Pauli blocking. The nucleons are perfectly localized in phase space and are bound by a constant potential. In this approach, the nuclear collision is treated as successive relativistic binary hadron-hadron collisions separated in time in which the positions and momenta of hadrons are followed as time evolves. Cross sections are determined from a set of collision events taken at different impact parameters, and for which baryon positions and momenta are initially sampled for each nucleus.

In this work, we use the latest C++ version of the Liège intranuclear cascade model INCL++ 6.0 [50], which is equivalent to the reference FORTRAN INCL4.6 version [66–68], but includes the formation of  $\Lambda$  hyperremnants. Hereafter, we will refer to this version as the INCL model, for simplicity. In this model, the hadron-nucleus reactions are modeled as a sequence of binary collisions between the nucleons (hadrons) present in the system. Nucleons move along straight trajectories until they undergo a collision with another nucleon or until they reach the surface, where they eventually escape. The latest version of the INCL also includes isospin- and energy-dependent nucleus potentials calculated according to

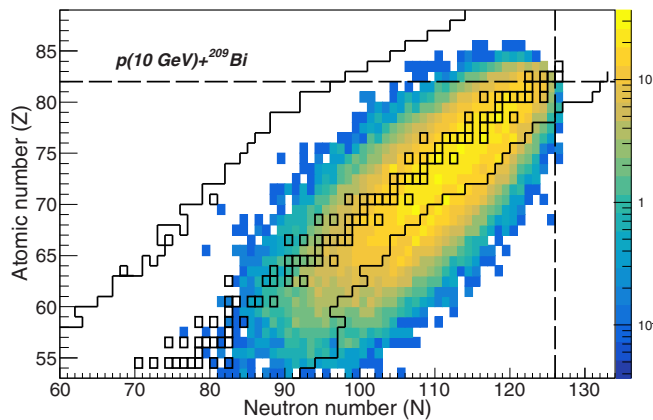


FIG. 1. Production cross sections (in mb) of hyperremnants in the reaction  $p(10 \text{ GeV})+^{209}\text{Bi}$  as a function of their atomic and neutron numbers. The open squares represent the stable nuclei and the solid contour lines indicate the region of known nuclei. The dashed lines are to indicate the magic numbers  $Z = 82$  and  $N = 126$ .

optical models [68], isospin-dependent pion potentials [69], as well as meson and strange particle potentials [47,49,50]. We emphasize that the parametrization of the  $\Lambda$  particle potential was changed with respect to our previous publications and in this work we use a potential of 30 MeV for symmetric nuclei, instead of the initial value of 28 MeV given in Refs. [49,50]. Additionally, Pauli principle is considered by means of statistical blocking factors and strict ones for the first nucleon-nucleon collision [43]. Finally, cluster emission is also possible via a dynamical phase-space coalescence algorithm [68].

Target density profiles are prepared at the first step of the simulation assuming independent Woods-Saxon density distributions for protons, neutrons, and  $\Lambda$  particles [49,70]. For the Woods-Saxon density distribution, the radius ( $R_0$ ) and the diffuseness parameter ( $a$ ) are taken from Hartree-Fock-Bogoliubov calculations [71]. Additionally, the nucleons are sampled in phase space, taking into account the correlations between kinetic energy and radius of the potential well [43], such that the relationship is given by the Woods-Saxon distribution.

In INCL, each event is started at a given impact parameter  $b$ , ranging from 0 to a distance  $b_{\text{max}}$  larger than the interaction distance between the projectile and target systems. During the cascade process, two types of nucleons (baryons if the nuclear system is a hypernucleus) are considered: spectators and participants. For the target, all the nucleons are considered spectators at the beginning of the collision and are forced to not interact with other nucleons in order to avoid the spontaneous boiling of the Fermi sea. When these nucleons are impinged by the projectile nucleons, they become participants. For the projectile system, all nucleons outside the overlap region of the projectile and target nuclear densities are considered geometrical spectators and the other ones participants. However, if a projectile participant does not interact with a target spectator, it becomes a dynamical spectator. The interaction between two nucleons takes place when they approach each other at a distance smaller than a

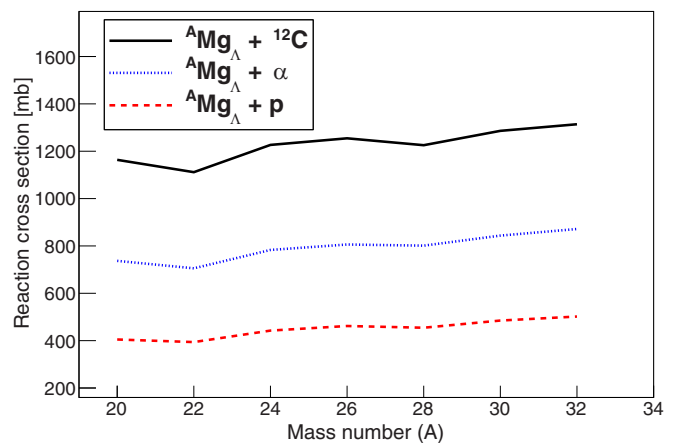


FIG. 2. Total reaction cross sections for different hypermagnesium isotopes impinging on carbon nuclei (solid line),  $\alpha$  (dotted line), and proton particles (dashed line) at kinetic energies of 1 A GeV.

minimum distance. This minimum distance is calculated from an energy-dependent parametrization of the baryon-baryon interaction cross section for  $pn$ ,  $pp$ , and  $nn$  collisions [72]. In the case of a hypernuclei-like target, it also includes the  $p\Lambda$  and  $n\Lambda$  interaction cross sections [48].

Figure 1 displays the production cross section in mb of hot hyperremnants produced in proton-induced spallation reactions on  $^{209}\text{Bi}$  at a kinetic energy of 10 GeV. The cross sections are represented as a function of the number of protons ( $Z$ ) and neutrons ( $N$ ) contained by the hot hyperremnants. As observed in the figure, most of the hot hyperremnants are produced around the stability region of normal stable nuclei, but there is also an important amount of neutron-rich hyperremnants produced beyond the limits of known normal nuclei that after the deexcitation decay processes may end as very neutron-rich hypernuclear systems. These hypernuclei are very interesting because they could be measured in the future state of the art experiments planned in some worldwide nuclear physics facilities like FAIR and HIAF.

INCL allows us to calculate the reaction cross section of any  $\Lambda$  hypernucleus impinging onto light particles, such as protons or neutrons, or light ions up to nuclei with a mass number smaller than  $A = 18$ . This is illustrated in Fig. 2 for different  $\Lambda$  hypernuclei of Mg isotopes impinging on proton (dashed line),  $\alpha$  (dotted line), and carbon nuclei (solid line). As expected, the reaction cross sections increase smoothly with the mass number of Mg isotopes since the size of the nuclear system also increases with the mass. The comparison of these calculations to experimental data would be used to investigate  $\Lambda$ -hypernuclei radii or the presence of neutron halos in very neutron-rich hypernuclei, like we do for normal nuclei [73,74]. In particular, this kind of measurement would be utilized to study the evolution of the hypernuclear shrinkage [75] with the mass asymmetry.

## B. Deexcitation model ABLA

For the deexcitation stage, we use the ABLA07 model [57] translated to C++, which describes the deexcitation of

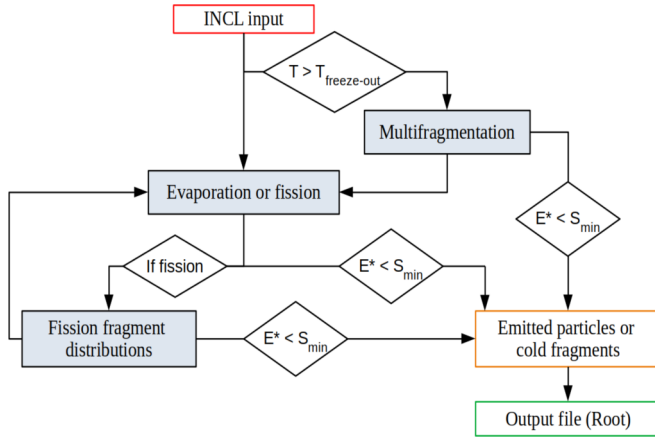


FIG. 3. ABLA diagram of deexcitation processes where  $E^*$  and  $T$  represent the excitation energy and temperature of the nuclear system, respectively,  $S_{\min}$  is the minimum particle separation energy, and  $T_{\text{freeze-out}}$  is the freeze-out temperature described in Sec. II B 1.

a nuclear system emitting  $\gamma$  rays, neutrons, light-charged particles, and intermediate-mass fragments (IMFs) or fission in case of hot and heavy remnants. The ABLA deexcitation diagram is displayed in Fig. 3. In the following, we will do an overview of the main features for describing each decay process, including the new ingredients for the strange sector.

### 1. Multifragmentation

If the excitation energy acquired during the collision phase is high enough to increase the volume of the nuclear system, this could reach the spinodal region characterized by a negative incompressibility [76]. In this region, an increase in the volume due to its expansion is directly connected with an increase in pressure and, consequently, any local fluctuation in density is strongly amplified, leading to a mixed phase consisting of droplets represented by a small amount of light nuclei at normal nuclear density and a nuclear gas composed of individual nucleons. This process is often called breakup. The fragments formed in this stage undergo the usual deexcitation processes and cool down. What is finally experimentally observed are the cold fragments, normally called intermediate fragments (IMFs). The starting point of the multifragmentation stage in ABLA is a hot nuclear system, the so-called spectator or remnant, left over from the initial collision stage. We assume that if the excitation energy per nucleon of the remnant exceeds a limiting value [77], the system undergoes the multifragmentation decay; otherwise the excited remnant will directly deexcite through sequential evaporation and/or fission. Note that the multifragmentation process is scientifically very interesting for its relation to the EOS of nuclear matter and, in particular, to the liquid-gas phase transition.

About the limiting excitation energy per nucleon or temperature, two options are possible in ABLA. By default, the multifragmentation stage is allowed only if the temperature of the remnants exceeds a mass-dependent freeze-out temperature threshold calculated according to the prescription given

by Natowitz and collaborators [78]:

$$T_{\text{freeze-out}} = \max[5.5, 9.33e^{(-2.82 \times 10^{-3} A^{\text{Rem}})}] \text{ MeV},$$

where  $A^{\text{Rem}}$  is the mass number of the remnant. If this temperature threshold is overcome, the system breaks up into a cocktail of fragments and nucleons whose mass is sampled according to an empirical power law written as

$$\frac{d\sigma}{dA} = A^{-\tau(E^*/A)},$$

whose slope is rather well modeled by an exponent  $\tau$  that depends on the mass number and excitation energy of remnants [79]. In this case, the parameter  $\tau(E^*/A)$  is described according to the parametrization given by Botvina and collaborators [80]. Therefore, the mass of nucleons and fragments produced at the breakup stage is sampled from an exponential distribution with a slope parameter  $\tau$ , providing that the sampled mass is rejected when exceeding the maximum available mass given as  $A^{\text{Max}} = A^{\text{Rem}} - A_{\text{freeze-out}}$ . Here,  $A_{\text{freeze-out}}$  corresponds to the freeze-out mass that is determined from the freeze-out temperature and the average energy removed per nucleon in the breakup process according to Ref. [77]. The value of  $\tau$  is calculated assuming a linear dependence on the excitation energy per nucleon in the temperature regime of interest, as explained in Refs. [79,80]. The sampling is performed until the maximum available mass  $A^{\text{Max}}$  is consumed. The atomic number of the corresponding fragment is also sampled at the same time from a Gaussian distribution centered at a value  $Z_{\text{mean}}$ , which is determined by imposing that the ratio  $A/Z$  is equal to that given by the hot remnant. The width of the distribution is given by

$$\sigma_Z^2 = \frac{T_{\text{freeze-out}}}{C_{\text{sym}}},$$

where  $C_{\text{sym}}$  is the symmetry term of the nuclear equation of state [81]. The excitation energies of the resulting hot residues are determined by assuming thermal equilibrium at the freeze-out temperature [77]. Finally, each of the breakup residues with a mass number greater than  $A = 4$  will then enter the particle evaporation process or fission if applicable. All the emitted particles and cold fragments (at ground state) produced during the multifragmentation process are stored in the output file, while the excited systems enter the particle decay process or fission if applicable.

Another possible option for the multifragmentation stage is to assume that the temperature is constant for all nuclei. In this case, its value is fixed to 5.5 MeV [77]. Both options can be selected in the ABLA configuration interface.

In the case of hyperremnants, we assume that the  $\Lambda$  particle can be treated as a neutron, being the probability of attaching to a fragment proportional to its number of neutrons. This means that at the end of the multifragmentation stage, we randomly choose the fragment that contains the  $\Lambda$  particle as a function of the fragment's neutron number. We will show later that this assumption works very well for the fission decay since we use experimental data to validate the approach.

## 2. Particle evaporation

The particle emission probabilities are calculated according to the Weisskopf-Ewing formalism [82] in which the decay width of a specific initial nucleus, characterized by its excitation energy (angular momentum)  $E_i$  ( $J_i$ ) into a daughter nucleus with excitation energy  $E_f$  ( $J_f$ ) by emission of a particle  $\nu$  with kinetic energy  $\epsilon_\nu$ , is given as

$$\Gamma_\nu(E_i) = \frac{(2\theta_\nu + 1)m_\nu}{\pi^2 \hbar^2 \rho_i(E_i, J_i)} \int_0^{E_i - S_\nu - B_\nu} \sigma_c(\epsilon_\nu) \rho_f(E_f, J_f) (\epsilon_\nu - S_\nu - B_\nu) dE_f,$$

where  $\theta_\nu$  is the spin of the emitted particle,  $\rho_i$  and  $\rho_f$  are the level densities in the initial and the daughter nucleus, respectively,  $\sigma_c$  is the cross section for the inverse process,  $S_\nu$  is the separation energy of the particle,  $B_\nu$  is the Coulomb energy or emission barrier (only for charged particles), and  $m_\nu$  is the mass of the emitted particle. For a more realistic description, the separation energies and the emission barriers for charged particles are considered according to the atomic mass evaluation from 2016 [83] and the prescription given by Qu and collaborators [84], respectively. In this new version of ABLA, we use Qu's approach instead of the Bass model [85] because both descriptions provide similar results for the emission barriers, but Qu's approach is much faster in the case of intermediate-mass and heavy remnants.

For hypernuclei, we have included in ABLA the calculation of the  $\Lambda$  particle separation energies according to the Bethe-Weizsäcker mass formula for hypernuclei (BWMH) developed by Samanta and collaborators [86]. In Figs. 4(a) and 4(b), we compare the results of this equation to experimental data of  $\Lambda$  hypernuclei [18,86] and to the approach used by the SMM model [87]. Additionally, we also display the results provided by the relativistic mean field model (RMF) developed by Hu and collaborators [88]. As can be seen in Fig. 4(a), the BWMH, SMM, and RMF calculations give similar results for the separation energies ( $S_n$ ) of light hypernuclei ( $A < 70$ ) and describe reasonably well the experimental data; however, the SMM approach systematically underestimates the experimental data of heavy hypernuclei. The same deviation can be observed in Fig. 4(b) for the two-neutron separation energies ( $S_{2n}$ ) of  $^{208}\text{Pb}$  nuclei as a function of the number of  $\Lambda$  hyperons. Consequently, and as we will show later, ABLA will predict larger probabilities of producing heavy hypernuclei.

For the calculation of the nuclear level density, different sophisticated models have been developed during the past decades. These models employ various techniques ranging from microscopic combinatorial methods [89] and Hartree-Fock approaches [90] to phenomenological analytical expressions [91]. On the one hand, it is desirable to model the nuclear density of states using a microscopic approach since it contains detailed information of nuclear levels. However, the amount of computing time needed for microscopic calculations limits the applicability of this approach. On the other hand, most of the studies related to nuclear reaction calculations prefer the analytical level density descriptions because they allow one to describe the experimental data very well for hundreds of different isotopes. In ABLA, two

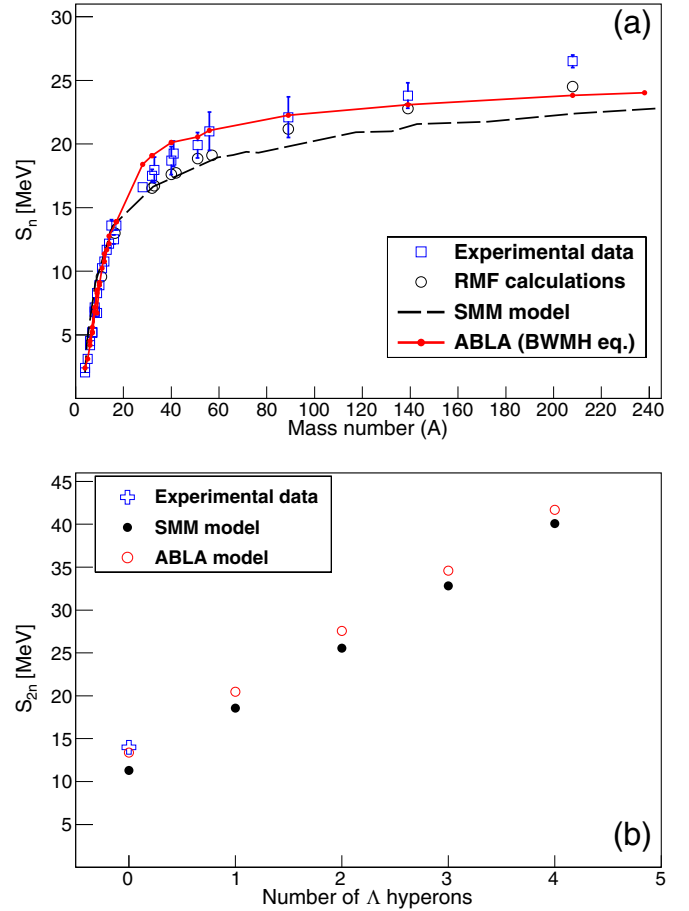


FIG. 4. (a) Separation energy of the  $\Lambda$  hyperon as a function of the hypernucleus mass number. The open squares are experimental data taken from Refs. [18,86] and the open circles represent RMF calculations [88]. The dashed line corresponds to the SMM model while the solid line represents results from the BWMH equation described in Ref. [86]. (b) Two-neutron separation energy for hypernuclei of  $^{208}\text{Pb}$  as a function of the number of  $\Lambda$  hyperons. Experimental data [83] is indicated with a cross.

phenomenological models, the constant temperature model of Gilbert-Cameron [92] and the Fermi gas model [93] based on the Bethe formula, are used in the level-density calculations. In these models, the excitation energy can be shifted to take the shell and pairing corrections according to Refs. [94,95] into account.

Following the Fermi gas model [93], the level density can be calculated as a function of the excitation energy  $E^*$  and the angular momentum  $J$  as

$$\rho(E^*, J) = \frac{J + 1/2}{\sqrt{2\pi} \sigma^3} e^{-\frac{J(J+1)}{2\sigma^2}} \frac{\sqrt{\pi}}{12} \frac{e^S}{\tilde{a}^{1/4} E^{*5/4}}, \quad (1)$$

where  $\sigma^2$  is the spin cutoff factor given by  $\sigma^2 = \frac{\Im T}{\hbar^2}$  with  $\Im$  as the moment of inertia of the nucleus and  $T$  as the nuclear temperature,  $E^*$  is the excitation energy of the system,  $S$  is the entropy, and  $\tilde{a}$  is the asymptotic level-density parameter in units of  $\text{MeV}^{-1}$ . At present, the most abundant information on level densities comes from the counting of low-lying levels and from neutron resonances [96,97]. These techniques

have also been extensively exploited to obtain the asymptotic level-density parameter ( $\tilde{a}$ ), which relates the nuclear temperature ( $T$ ) with the excitation energy ( $E^*$ ) according to  $E^* = \tilde{a}T^2$ , and to investigate the evolution of  $\tilde{a}$  with the excitation energy [98]. Generally, this last parameter can be written as [99,100]

$$\tilde{a} = \alpha_v A + \alpha_s B_s A^{2/3} + \alpha_k B_k A^{1/3},$$

where  $A$  is the mass of the nucleus and  $\alpha_v$ ,  $\alpha_s$ , and  $\alpha_k$  are the coefficients that correspond to the volume, surface, and curvature components of the single-particle level densities, respectively. The values of these coefficients were calculated by Ignatyuk [100] ( $\alpha_v = 0.095$ ,  $\alpha_s = 0.073$ , and  $\alpha_k = 0$  in units of  $\text{MeV}^{-1}$ ) and are the most frequently used in model calculations. In the equation,  $B_s$  represents the ratio between the surface of the deformed nucleus and a spherical nucleus while  $B_k$  corresponds to the ratio between the integrated curvature of the deformed nucleus and a spherical nucleus. Their parametrizations are taken from Ref. [101].

The entropy  $S$  is obtained according to the equation

$$S = 2\sqrt{\tilde{a}E_{\text{mod}}^*} = 2\sqrt{\tilde{a}[E^* + \Delta U k(E^*) + \Delta P h(E^*)]}, \quad (2)$$

where  $\Delta U$  is the shell-correction energy, which is calculated according to Ref. [95] for excited nuclear systems. At the fission saddle point, the shell-correction energy is assumed to be negligible [102,103]. The term  $k(E^*)$  describes the damping of the shell effect with the excitation energy, and is calculated according to Ref. [98] as

$$k(E^*) = 1 - e^{-\gamma E^*},$$

with the parameter  $\gamma$  given by  $\gamma = \tilde{a}/(0.4A^{4/3})$  in units of  $\text{MeV}^{-1}$  [104]. The term  $\Delta P$ , which is identical to the pairing condensation energy in odd-odd nuclei, is calculated as

$$\Delta P = 2\delta + 1/4g\delta^2,$$

with an average pairing gap of  $\delta = 12/\sqrt{A}$  in units of MeV, and with a single-particle level density at the Fermi energy of  $g = 6\tilde{a}/\pi^2$ . Finally, the term  $h(E^*)$  describes the superfluid phase transition [94] according to Ref. [105] as

$$h(E^*) = \begin{cases} 1 - (1 - \frac{E^*}{E_{\text{crit}}})^2 & \text{if } E^* < E_{\text{crit}} \\ 1 & \text{if } E^* \geq E_{\text{crit}} \end{cases},$$

where the critical energy ( $E_{\text{crit}}$ ) is set to 10 MeV. Note that in these equations the excitation energy is shifted according to the prescription given in Ref. [57] to accommodate for the different energies of even-even, odd-mass, and odd-odd nuclei.

In order to calculate the intrinsic level density at very low excitation energies, ABLA switches from the Fermi-gas level density to the constant-temperature level density [92]. The calculation is based on the work performed in Ref. [106], where the values of the parameters of the constant-temperature level density approach were obtained from the simultaneous analysis of the neutron resonances and the low-lying levels in the framework of the Gilbert-Cameron approach [92].

To account for the role of collective excitations in the decay of excited compound nuclei, the level density of Eq. (1) is

corrected using the vibrational and rotational enhancement factors according to

$$\rho(E, J) = K_{\text{vib}} K_{\text{rot}} \rho(E, J)_{\text{int}},$$

where  $\rho(E, J)_{\text{int}}$  is given by Eq. (1),  $K_{\text{vib}}$  represents the vibrational enhancement factor, and  $K_{\text{rot}}$  corresponds to the rotational factor. For nuclei with highly deformed deformation, the collective enhancement factor arises from the appearance of rotational bands above the intrinsic single-particle levels. In this case, the vibrational factor  $K_{\text{vib}}$  can be thus considered negligible while the rotational enhancement factor is calculated according to Refs. [107,108] in terms of the rigid-body moment of inertia. By contrast, for spherical nuclei the collective motion is calculated on the basis of low-frequency vibrational modes. At present, the factor  $K_{\text{vib}}$  can be calculated from the statistical sum of harmonic vibrational modes [107] or by using phenomenological approaches [109]. In ABLA, these factors are calculated according to the phenomenological description proposed by Junghans and collaborators [109].

For nuclei with a quadrupole deformation  $|\beta_2| > 0.15$ , the rotational enhancement factor  $K_{\text{rot}}(E_{\text{mod}}^*)$  is calculated in terms of the spin-cutoff parameter  $\sigma_{\perp}$ :

$$K_{\text{rot}}(E_{\text{mod}}^*) = \begin{cases} 1 + (\sigma_{\perp}^2 - 1)f(E_{\text{mod}}^*) & \text{if } \sigma_{\perp} > 1 \\ 1 & \text{if } \sigma_{\perp} \leq 1 \end{cases}, \quad (3)$$

being  $\sigma_{\perp}^2 = \frac{\mathfrak{I}_{\perp} T}{\hbar^2}$ , where  $T$  is the temperature of the nuclear system and  $\mathfrak{I}_{\perp}$  is the rigid-body moment of inertia perpendicular to the symmetry axis determined according to Ref. [110]. In this expression,  $E_{\text{mod}}^*$  is defined by Eq. (2). The ground-state quadrupole deformation  $\beta_2$  is taken from the finite-range liquid-drop model including microscopic corrections [95], while the saddle-point deformation is taken from the liquid-drop model as given in Ref. [111]. The damping of the collective modes with increasing excitation energy [ $f(E_{\text{mod}}^*)$ ] is described by a Fermi function as

$$f(E_{\text{mod}}^*) = \left(1 + e^{\frac{E_{\text{mod}}^* - E_c}{d_c}}\right)^{-1},$$

with the parameters  $E_c = 40 \text{ MeV}$  and  $d_c = 10 \text{ MeV}$ . The vibrational enhancement for spherical nuclei is generally smaller than the rotational enhancement for deformed nuclei. For nuclei with a quadrupole deformation  $|\beta_2| \leq 0.15$ , the vibrational enhancement factor is calculated by using the same formula as for the rotational enhancement [Eq. (3)], but with the spin-cutoff parameter calculated assuming an irrotational flow:

$$\sigma_{\perp}^2 = 75\beta_{\text{eff}}\sigma_{\perp}^2,$$

where  $\beta_{\text{eff}}$  is a dynamical deformation parameter expressed as  $\beta_{\text{eff}} = 0.022 + 0.003\Delta N + 0.002\Delta Z$ , with  $\Delta N$  and  $\Delta Z$  being the absolute values of the number of neutrons and protons, respectively, above or below the nearest shell closure.

In the standard Weisskopf-Ewing approach [82], the change of angular momentum in the evaporation process due to particle emission is not treated. To overcome this limitation, a dedicated formalism according to Ref. [57] is included in ABLA to calculate the distribution of orbital angular

momentum during the emission of particles from the excited nuclear systems with a finite angular momentum.

Finally, the inverse cross section ( $\sigma_c$ ) for the emission of particles is calculated considering several effects: The existence of the Coulomb barrier for charged particles (especially at low energy), the tunneling through it (especially for light particles), and the energy-dependent quantum-mechanical cross section. Knowing that at energies well above the Coulomb barrier the shape of the barrier does not play any role,  $\sigma_c$  can then be calculated without taking into account the tunneling as [57]

$$\sigma_c(\epsilon_\nu) = \pi \left( 1.16(A_1^{1/3} + A_2^{1/3}) + \sqrt{\frac{\hbar^2}{2\mu E_{c.m.}}} \right)^2 \left( 1 - \frac{B_\nu}{\epsilon_\nu} \right),$$

where  $\mu$  is the reduced mass, calculated as  $\mu = M_1 M_2 / (M_1 + M_2)$ , and  $E_{c.m.} = \epsilon_\nu (A_1 - A_2) / A_1$ .

### 3. $\gamma$ -ray emission

Usually deexcitation codes do not include the  $\gamma$  radiation as a possible emission channel since particle decay channels dominate above the particle-emission threshold. However, in the last deexcitation stage of the evaporation cascade,  $\gamma$  emission becomes competitive to particle decay for compound nuclei. Normally, the emission of  $\gamma$  rays is much less probable than the particle decay (about  $10^5$  times less favorable). Since the level density depends on the mass (heavier nuclei have denser energy levels), the number of levels between the ground state and the particle separation energy of a heavy nucleus can be as high as  $10^5$  or even exceed this value. If the excitation energy of the compound nucleus is slightly higher than its particle separation energy, it can decay only into the ground state or into the first excited states of the daughter nucleus (if the daughter nucleus is an even-even nucleus, then only the ground state is energetically accessible due to the pairing gap; see, for instance, Ref. [112] for a wider discussion). In this situation,  $\gamma$ -ray emission and particle decay can thus become two competitive channels.

As the emission of statistical  $\gamma$  rays occurs predominantly via the giant dipole resonance, the  $\gamma$ -radiation rate can be calculated according to Ref. [106]. Assuming the power approximation for the radiative strength function [113] and the constant-temperature model [106], the  $\gamma$ -radiation rate can be parameterized as

$$\Gamma_\gamma(T) = 0.624 \times 10^{-9} A^{1.6} T^5,$$

where  $A$  is the mass of a mother nucleus and  $T$  is the nuclear-temperature parameter of the constant-temperature model. The effects of  $\gamma$ -ray decay are especially visible in the strength of the even-odd staggering of the final products as shown in Ref. [112].

### 4. Fission decay

Fission plays an important role in the decay of heavy nuclei. At each deexcitation stage, a competition between fission and other decay channels is calculated. In ABLA, the fission decay width is described by the Bohr-Wheeler (BW) transition-state model [114] following the formulation given

by Moretto [115]:

$$\Gamma_f^{BW} = \frac{T}{2\pi} \frac{\rho_{sp}(E - B_f, J)}{\rho_{gs}(E, J)}, \quad (4)$$

where  $\rho_{sp}(E - B_f, J)$  and  $\rho_{gs}(E, J)$  are the level densities at the saddle-point and ground-state configurations, respectively,  $T$  is the nuclear temperature, and  $B_f$  is the fission-barrier height obtained from the finite-range liquid-drop model of Sierk [116] taking into account the influence of angular momentum and considering the ground-state shell effects [95].

The diffusion process above the fission barrier is described by the Fokker-Planck equation, where the quasistationary solution of this equation was introduced by Kramers [117] and provides a reduction of the fission decay width due to dissipation:

$$\Gamma_f^K = \left[ \sqrt{1 + \left( \frac{\beta}{2\omega_0} \right)^2} - \frac{\beta}{2\omega_0} \right] \Gamma_f^{BW}.$$

Here  $\beta$  is the dissipation coefficient and  $\omega_0$  is the frequency of the harmonic oscillator describing the inverted potential at the fission barrier, calculated according to the liquid-drop model [118]. This equation provides the asymptotic value of the fission decay width, which is modified according to an analytical approximation to the solution of the one-dimensional Fokker-Planck equation [119] developed by Jurado and collaborators in Refs. [120,121] to take into account the time dependence of the fission-decay width. This description was modified later to consider the initial quadrupole deformation of compound nucleus as well, which results in a more realistic description of fission process in the actinide region [122]. Under this approximation, the time-dependent fission-decay width is defined as

$$\Gamma_f(t) = \frac{W_n(x = x_{sd}; t, \beta)}{W_n(x = x_{sd}; t \rightarrow \infty, \beta)} \Gamma_f^K,$$

where  $W(x; t, \beta)$  is the normalized probability distribution at the saddle-point deformation  $x_{sd}$ , being the saddle-point deformations calculated according to Ref. [110].

In the case of a nuclear potential approximated by a parabola, the solution of the Fokker-Planck equation for the probability distribution  $W(x; t, \beta)$  at the saddle-point deformation has a Gaussian form with a time-dependent width [123]. The zero-point motion is taken into account by shifting the timescale by a certain amount  $t_0$ , which is the time needed for the probability distribution to reach the width of the zero-point motion in deformation space. This time is calculated as [120]

$$t_0 = \begin{cases} \frac{1}{\beta} \ln \left( \frac{2T}{2T - \hbar\omega_1} \right) & \text{if } \beta \leq 2\omega_1 \\ \frac{\hbar\beta}{4\omega_1 T} & \text{if } \beta > 2\omega_1 \end{cases}$$

where  $\omega_1$  describes the curvature of the potential at the ground state.

This then leads to the following analytical approximation to the solution of the Fokker-Planck equation for the time-

dependent fission width:

$$\Gamma_f(t) = \frac{K_B T}{\mu \omega_1^2 \sigma^2} \frac{e^{-\frac{(x_{\text{sd}} - x_m)^2}{2\sigma^2}}}{e^{-\frac{\mu \omega_1^2 x_{\text{sd}}^2}{2K_B T}}} \Gamma_f^K,$$

with  $\sigma^2$  given as

$$\sigma^2 = \frac{K_B T}{\mu \omega_1^2} \left[ 1 - e^{-\beta(t+t_0)} \left( \frac{2\beta^2}{\beta_1^2} \sinh^2(0.5\beta_1(t+t_0)) + \frac{\beta}{\beta_1} \sinh(\beta_1(t+t_0)+1) \right) \right],$$

where  $K_B$  is Boltzmann's constant,  $\mu$  is the reduced mass associated to the deformation degree of freedom, and  $\beta_1 = (\beta^2 - 4\omega_1^2)^{1/2}$ . The dissipation coefficient  $\beta$  is fixed to  $4.5 \times 10^{-21} \text{ s}^{-1}$  since this value was constrained in many works [122,124–126]. Finally, the mean deformation  $x_m$  of the system is obtained as

$$x_m = \begin{cases} X_i \cos[0.5\beta_2(t-t_0)] e^{-\beta(t-t_0)} & \text{if } \beta \leq 2\omega_1 \\ X_i e^{-0.5(\beta-\beta_1)(t-t_0)} & \text{if } \beta > 2\omega_1 \end{cases},$$

being the initial deformation  $X_i$  calculated according to Ref. [101].

In the case of low-energy fission, the double-humped structure in the fission barrier as a function of elongation and the symmetry classes at different saddle points are of importance for a proper description of the process. These effects have also been included in the ABLA model [57], following the ideas developed in Refs. [127–129].

For the deexcitation of hyperremnants by fission, we do not expect any change either in the nuclear level density properties or in the fission mechanism for two reasons: The number of hyperons absorbed by the remnants is about one and the hyperremnants are produced with excitation energies above 50 MeV, where the hypercompound system can be considered as a Fermi gas. Therefore, fission of hypercompound systems is described as for normal nuclei, taking into account the hyperenergy released in the process that will contribute mainly to the fission barrier height. Similar to the SMM approach [87,130], in the case of hypercompound systems the hyperenergy contribution  $\Delta B_f^{\text{hyp}}$  released during the fission process due to the attractive  $YN$  force is added to  $B_f$  in Eq. (4). This hyperenergy  $\Delta B_f^{\text{hyp}}$  is parametrized according to the description given by Ion and collaborators [131] as follows:

$$\Delta B_f^{\text{hyp}} = 0.51(m_\Lambda - m_n + S_n - S_\Lambda)/A^{2/3},$$

where  $m_\Lambda$  ( $S_\Lambda$ ) and  $m_n$  ( $S_n$ ) are the  $\Lambda$  and neutron masses (separation energies), respectively, and  $A$  is the mass number of the hypercompound nucleus. This equation leads to small increases in the fission barrier height up to  $\Delta B_f \approx 1 \text{ MeV}$  that are, for instance, compatible with the results obtained from more sophisticated calculations based on Skyrme-Hartree-Fock approaches [132].

### 5. Fission fragment distribution

Properties of fission fragments, i.e., masses, atomic numbers, and excitation and kinetic energies, are calculated based

on the macro-microscopic approach and the separability of compound nucleus and fragment properties along the fission path [133]. The original technical description of the fission fragment properties was published in Refs. [134,135], in which we assume that the different splits in mass are basically determined by the number of available transition states above the potential energy surface behind the outer saddle point. The macroscopic properties of the potential-energy landscape of the fissioning system are attributed to the strongly deformed fissioning system, which are deduced from mass distributions at high excitation energy [136] and Langevin calculations [137]. At high excitation energies, the fission process is dominated by the symmetric fission, the so-called superlong fission channel, which can be explained by the macroscopic properties of the potential-energy landscape of the fissioning nucleus at the saddle point. In particular, the stiffness of the macroscopic potential along the mass-asymmetry degree of freedom is obtained from the systematics of the width of mass distributions measured in Ref. [136]. The neutron-to-proton ratio ( $N/Z$ ) of the fission fragments is assumed to be given by the unchanged-charge distribution (UCD). This  $N/Z$  ratio is then modified by the charge polarization effect calculated in terms of the liquid-drop model (LDM) by assuming a configuration of two touching spheres at the scission point [138] and by the evaporation of particles during the descent from the saddle to scission configuration [139]. On the other hand, the microscopic properties of the potential-energy landscape of the fissioning system are given by the qualitative features of the shell structure in the nascent fragments. They are determined from the observed features of the fission channels [140] according to the procedure described in Ref. [135].

According to the statistical model [141], the widths of the mass and atomic-number distributions of the fission fragments,  $\sigma_A$  and  $\sigma_Z$  respectively are related to the temperature at the saddle point according to the equations

$$\sigma_A^2 = \frac{A_{\text{fiss}}^2 T_{\text{sad}}}{16d^2V/dv^2} \quad \text{and} \quad \sigma_Z^2 = \frac{Z_{\text{fiss}}^2 T_{\text{sad}}}{16d^2V/dv^2},$$

where  $d^2V/dv^2$  is the second derivative of the potential with respect to the mass-asymmetry degree of freedom at the saddle point  $v = (4/A_{\text{fiss}})/(M - A_{\text{fiss}}/2)$ .  $A_{\text{fiss}}$  and  $Z_{\text{fiss}}$  correspond to the mass and atomic numbers of the fissioning nucleus, respectively, and  $M$  represents the mass number of the corresponding fragment. Due to the higher probability of neutron evaporation compared to proton emission beyond the saddle-point configuration, the width of the atomic-number distribution of the fission fragments ( $\sigma_Z$ ) is more suitable to constrain the temperature at the saddle point. In this sense, many experimental investigations have been performed at the GSI facility in the past decade with stable and exotic nuclei to measure the charge distributions of the fission fragments [120,122,124,125] and validate this approach.

The kinetic energies of the fission fragments are then calculated according to the semistatistical scission point model of Wilkins and collaborators [142]. The main contribution to the total kinetic energies released in the fission process comes from the Coulomb repulsion of the two fission fragments at

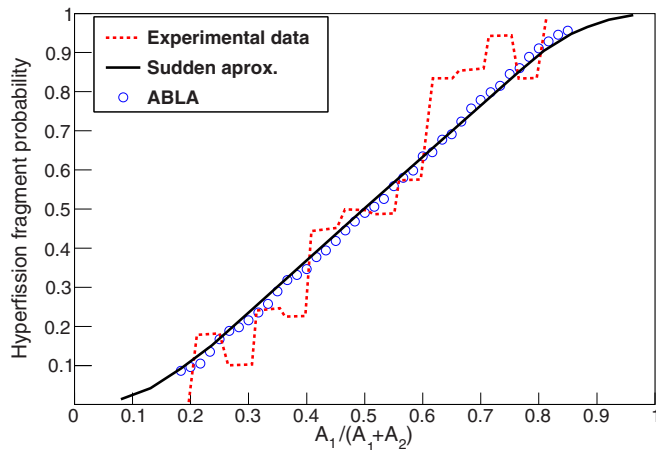


FIG. 5. Probability of producing hyperfission fragments as a function of the reduced mass  $A_1/(A_1 + A_2)$  assuming initial fissioning systems with a mass of  $A = 200$ , excitation energy of 50 MeV, and a single  $\Lambda$  hyperon inside the nuclear system according to the expected experimental conditions given in Ref. [146]. ABLA predictions (open circles) are also compared to experimental data [144,145] (dotted line) and model calculations based on the sudden approximation [146] (solid line).

the scission point and, therefore, this total kinetic energy is given by

$$\text{TKE} \sim \frac{Z_1 Z_2}{D},$$

where  $Z_1$  and  $Z_2$  refer to the atomic number of the two fission fragments, and  $D$  is the distance between the two uniformly charged spheroids representing the fission fragments. This distance is parametrized as

$$D = r_0 A_1^{*1/3} \left(1 + \frac{2\beta_1}{3}\right) + r_0 A_2^{*1/3} \left(1 + \frac{2\beta_2}{3}\right) + d,$$

where  $A_1^*$  and  $A_2^*$  refer to the mass number of the two fission fragments at the scission point,  $\beta_1$  and  $\beta_2$  are their quadrupole deformations at the scission point,  $r_0$  is the Fermi radius, and  $d$  is the distance between the tips of the two fission fragments. This distance  $d$  is fixed to 2 fm according to Ref. [143].

Finally, the two fission fragments are characterized by their atomic numbers  $Z_{1,2}$ , mass numbers  $A_{1,2}$ , kinetic energies  $E_{\text{kin}}^{1,2}$ , excitation energies  $E_{1,2}^*$ , and angular momenta  $J_{1,2}$  at the scission point. After this, their corresponding deexcitation chains are followed until their excitation energies fall below the lowest particle-emission threshold. In the case of dealing with hyperfragments, these are also characterized by their strangeness numbers  $I_s^{1,2}$ .

If a hyperremnant enters the fission decay, the  $\Lambda$  particle is treated as a neutron and thus the probability of attaching to a fission fragment is considered to be proportional to its number of neutrons. This means that we randomly choose the fission fragment that contains the  $\Lambda$  particle as a function of its neutron number. The results of this assumption for the average  $\Lambda$  attaching probability are displayed in Fig. 5 as a function of the reduced mass  $A_1/(A_1 + A_2)$ . Additionally, we also compare our calculations to the experimental data

obtained by Armstrong and collaborators [144,145] for hypernuclei formed in antiproton annihilation on  $^{238}\text{U}$  nuclei and to calculations based on the sudden approximation [146]. As can be observed, the  $\Lambda$  particle predominantly sticks to the heavier fission fragment, validating our assumption. Moreover, our calculations clearly provide a reasonable description of the experimental data and are also compatible with the sudden approximation, although in our case the calculations are based on a Monte Carlo technique.

### III. RESULTS

The INCL+ABLA model calculations have been evaluated in several works based on comparisons with nucleon-induced reactions on different nuclei between carbon and uranium at incident energies from a few MeVs to 10 GeV, providing a satisfactory description of many observables such as isotopic distributions of evaporation and fission residues [58,64,67,125,147–151], double differential cross sections [43,58,67,68,152], total reaction and fission cross sections [43,67,68,124,126,153,154], and meson production [43,45,69]. Since the ABLA07 deexcitation model has been translated to C++, it is important to demonstrate that the new C++ version still provides the same results. Like in previous publications, we use for benchmarking the model the reactions  $p + ^{136}\text{Xe}$  [155],  $p + ^{208}\text{Pb}$  [156,157], and  $p + ^{238}\text{U}$  [147,158] at 1A GeV. As shown in Fig. 6, both versions of ABLA coupled to INCL provide the same cross sections for fragment production. More calculations have been performed to validate the new version of ABLA, although they are not shown here. Simultaneously, in Fig. 6 we also display INCL+SMM model calculations in which one can see that the de-excitation model SMM underestimates the cross sections of medium-mass fragments produced via fission and multifragmentation reactions on projectiles of  $^{208}\text{Pb}$  and  $^{238}\text{U}$ . This was also pointed out by the benchmarks performed by the IAEA Collaboration some years ago and clearly explains why we have decided to extend the deexcitation model ABLA to the strange sector including the formation of  $\Lambda$  hypernuclei.

At the beginning, it is important to demonstrate that the different deexcitation mechanisms, such as evaporation, multifragmentation, and fission, are connected with each other in real disintegration processes for normal and hyperremnants. This can be done by comparing the probabilities of evaporation and fission processes since these observables can be easily obtained experimentally and are often used for validating model calculations. In Figs. 7(a) and 8(a), we display the evolution of these probabilities for  $^{209}\text{Bi}$  and  $^{238}\text{U}$  compound nuclei with their excitation energy, while in Figs. 7(b) and 8(b) we represent these probabilities for  $^{209}\text{Bi}$  and  $^{238}\text{U}$  compound hypernuclei, respectively. For normal compound nuclei, fission means that the nuclei undergo fission during the deexcitation process, while the label evaporation residue means that only emission of light nucleons and clusters took place during the de-excitation process. In the case of hypercompound nuclei, hyperfission means that at least one of the final fission fragments contains a  $\Lambda$  particle,  $\Lambda$  residues correspond to evaporation residues containing a  $\Lambda$  particle,

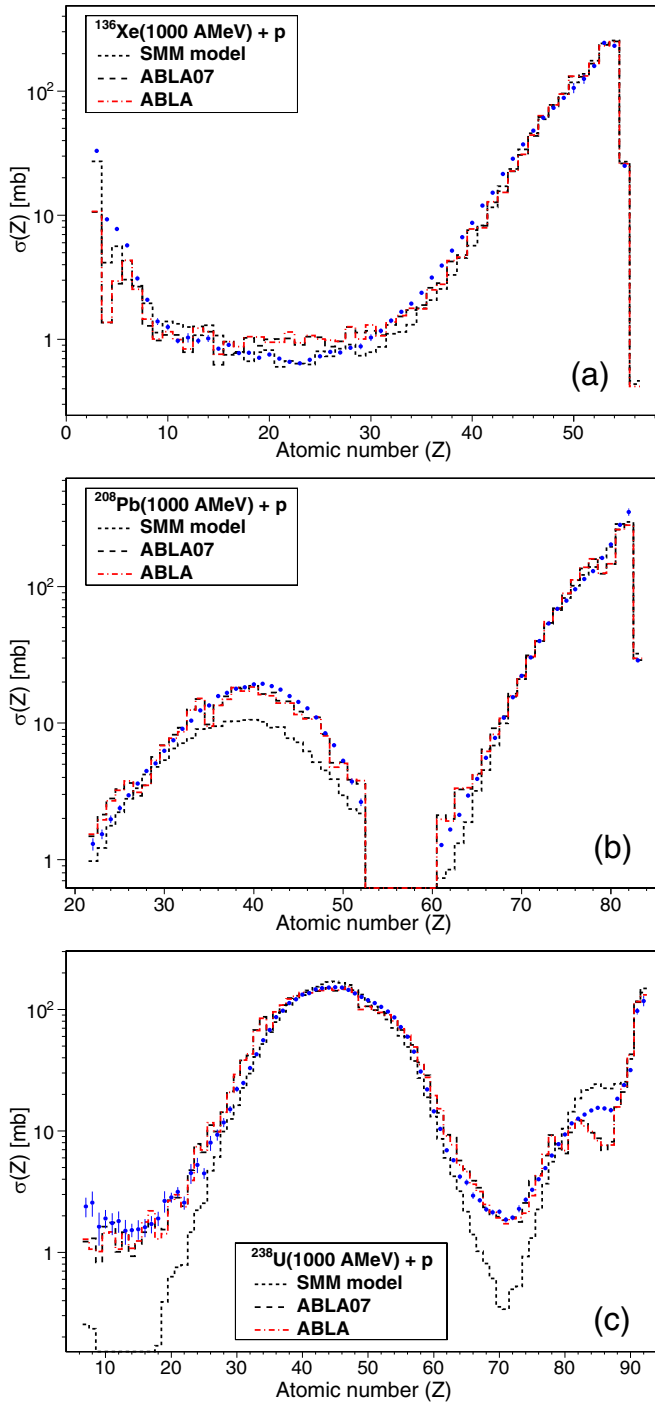


FIG. 6. Comparison of INCL+ABLA07 (dashed lines), INCL+ABLA (dash-dotted lines), and INCL+SMM (dotted lines) model calculations to nuclei production (solid circles) in proton-induced reactions on  $^{136}\text{Xe}$  [155] (a),  $^{208}\text{Pb}$  [156,157] (b), and  $^{238}\text{U}$  [147,158] (c) at 1A GeV.

and the label evaporation of  $\Lambda$  particles means that the  $\Lambda$  particle was emitted during the deexcitation process.

Our model calculations are compared to SMM predictions, providing similar results, although one can see some clear differences in the evolution of normal fission probabilities with the excitation energy. At low excitation energies, ABLA

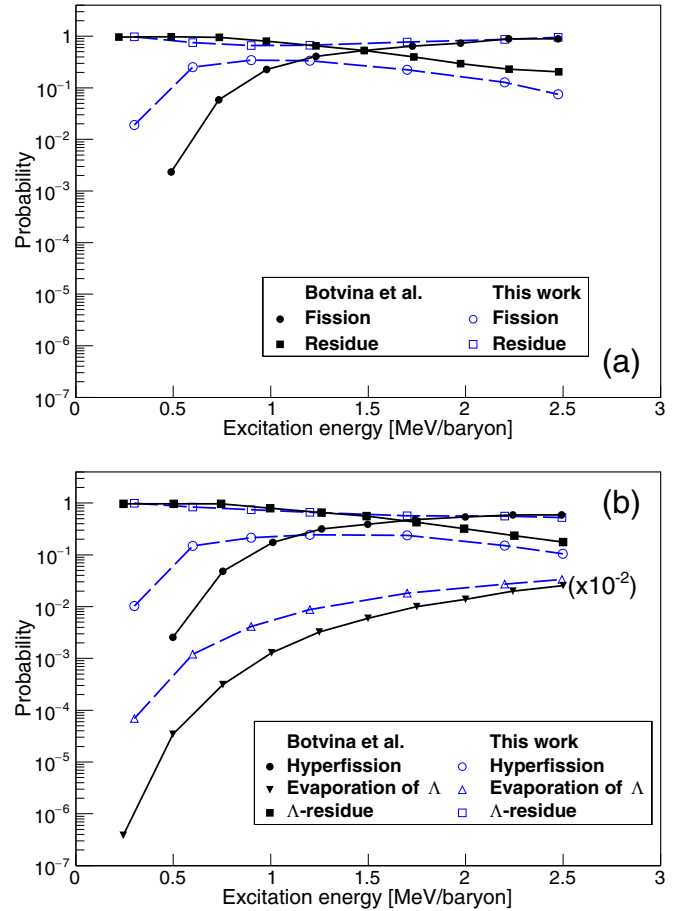


FIG. 7. (a) Probability of nuclear fission (circles) and evaporation residues surviving to the emission of light particles (squares) calculated with ABLA and SMM models for  $^{209}\text{Bi}$  compound nuclei as a function of the excitation energy per baryon. (b) Probability of the hypernuclear fission (circles) and surviving hypernucleus (squares) for  $^{209}\text{Bi}$  compound hypernuclei as a function of the excitation energy per baryon. The triangles represent the probability for emission of single  $\Lambda$  particles. Note that open symbols are for this work and solid ones are for SMM model calculations [87].

provides higher probabilities than the SMM model, and at high excitation energies, the fission probabilities decrease with respect to SMM predictions. This trend can be explained by a better description of the fission process at low excitation energies and the account of transient time effects at high excitation energies ( $E^* > 1.5 \text{ MeV/A}$ ) that reduce the fission probabilities as already demonstrated in different works with normal nuclear systems [121,122,124,125]. Similar trends are observed for hyperfission probabilities.

For a further benchmark, we also compare our model calculations to experimental data. The production of  $\Lambda$  residues can be validated, for instance, with single strangeness-exchanging ( $\pi^+$ ,  $K^+$ ) cross sections measured by the KEK Collaboration at Japan [159,160] (dots), which are displayed in Fig. 9 as a function of the target mass number ( $A$ ). We also include the data measured by the Brookhaven National Laboratory (BNL) [161] (open circles) and Compact Muon Solenoid (CMS) [159] (open squares) Collaborations

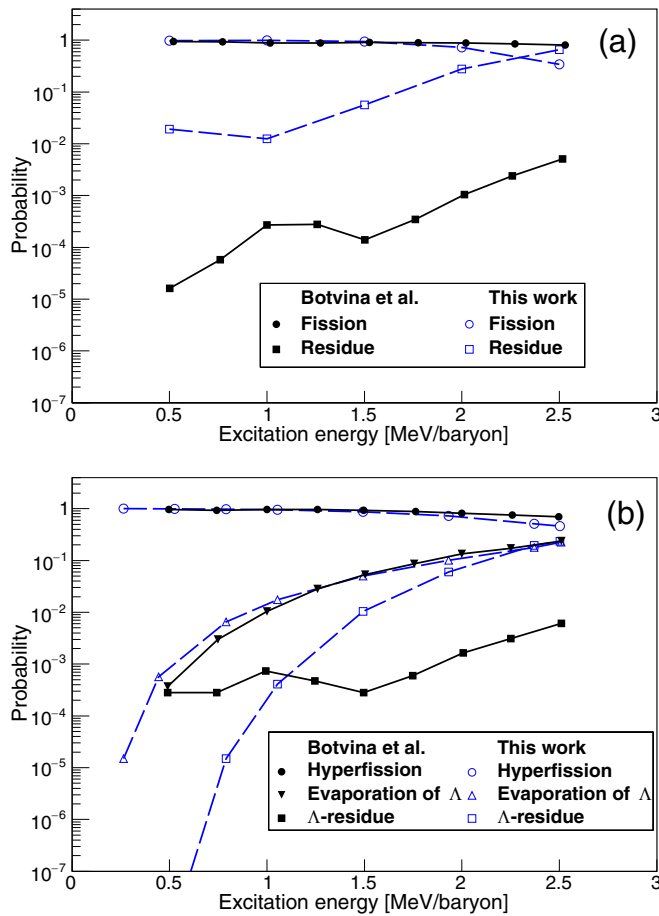


FIG. 8. The same as Fig. 7, but for  $^{238}\text{U}$  and  $^{238}_{\Lambda}\text{U}$  compound systems.

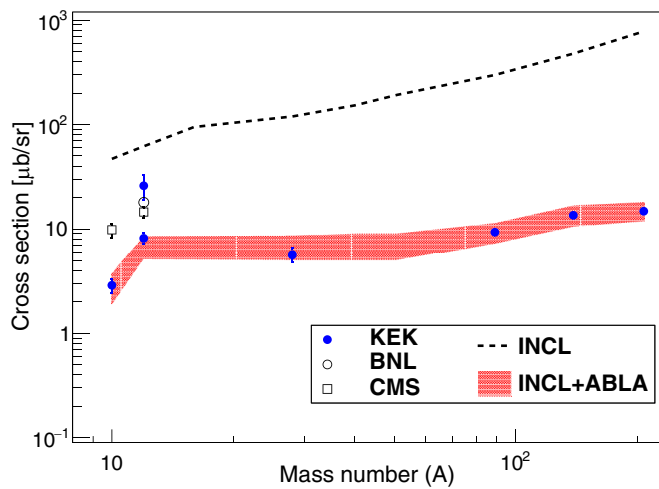


FIG. 9. Hypernuclear production cross sections in strangeness-exchanging ( $\pi^+$ ,  $K^+$ ) reactions as a function of the target mass number ( $A$ ) obtained by the KEK [159,160] (dots), BNL [161] (open circle), and CMS [159] (open squares) Collaborations. The data are compared to INCL (dashed line) and INCL+ABLA (dashed area) calculations.

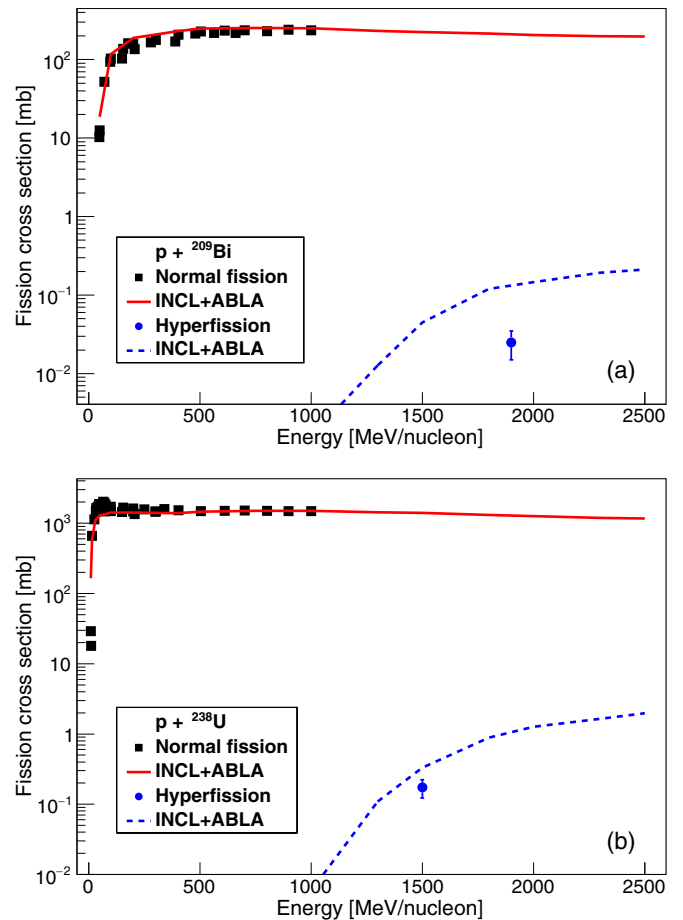


FIG. 10. Fission cross sections of normal remnants (squares) and hyperremnants (dots) produced in proton-induced fission reactions on  $^{209}\text{Bi}$  (a) and  $^{238}\text{U}$  (b) as a function of the projectile kinetic energy. Experimental data taken from Refs. [162–164] are compared to INCL+ABLA calculations for normal nuclear fission (solid lines) and hyperfission (dashed lines).

to show the experimental discrepancies that these cross sections present in the region of light nuclei, which can reach a factor of 10. These experimental data are compared to INCL calculations considering only the production of single strangeness-exchanging hyperremnants (dashed line) and to INCL+ABLA calculations (dashed area), which account for the emission of  $\Lambda$  particles from the hot hyperremnants. Note that the width of the dashed area represents the statistical uncertainty. One can see that there is a factor of 10–100 between both model calculations, as well as the evaporation of  $\Lambda$  particles is essential to describe the experimental cross sections. This result also demonstrates that the evaporation of  $\Lambda$  particles is well described in ABLA.

Another interesting deexcitation process that we can use for the benchmark is the hyperfission cross section. In Figs. 10(a) and 10(b), we display the experimental cross sections obtained for normal fission and hyperfission of  $^{209}\text{Bi}$  and  $^{238}\text{U}$ , respectively. The hyperfission of these nuclei was measured at the COSY-Jülich facility using the recoil shadow method [163,164]. As demonstrated in Ref. [151],

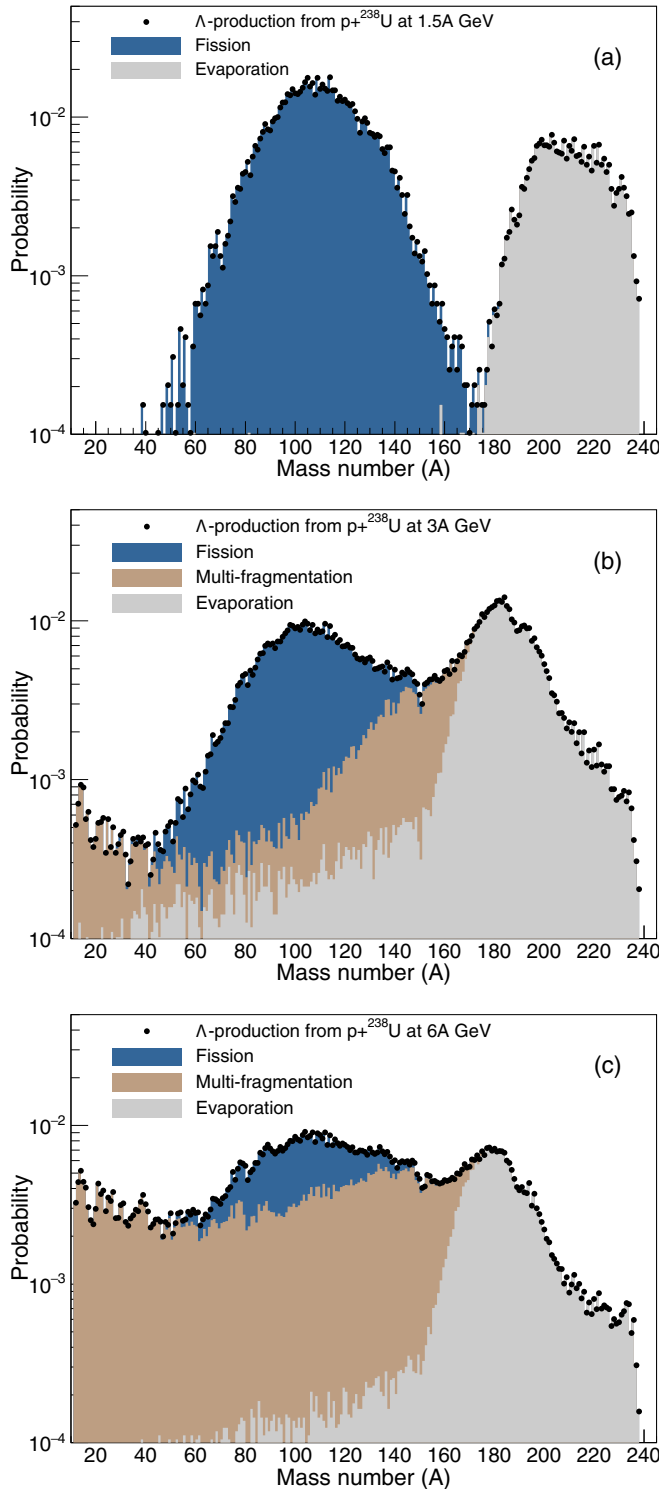


FIG. 11.  $\Lambda$ -hypernuclei probability (dots) as a function of the hypernuclei mass number ( $A$ ) for proton-induced reactions on  $^{238}\text{U}$  at 1.5A GeV (a), 3.0A GeV (b), and 6.0A GeV (c). The shadowed histograms represent the contributions from different decay processes, such as particle emission or evaporation, multifragmentation, and fission.

INCL+ABLA calculations (solid lines) provide a satisfactory description for the fission cross sections of normal nuclei as

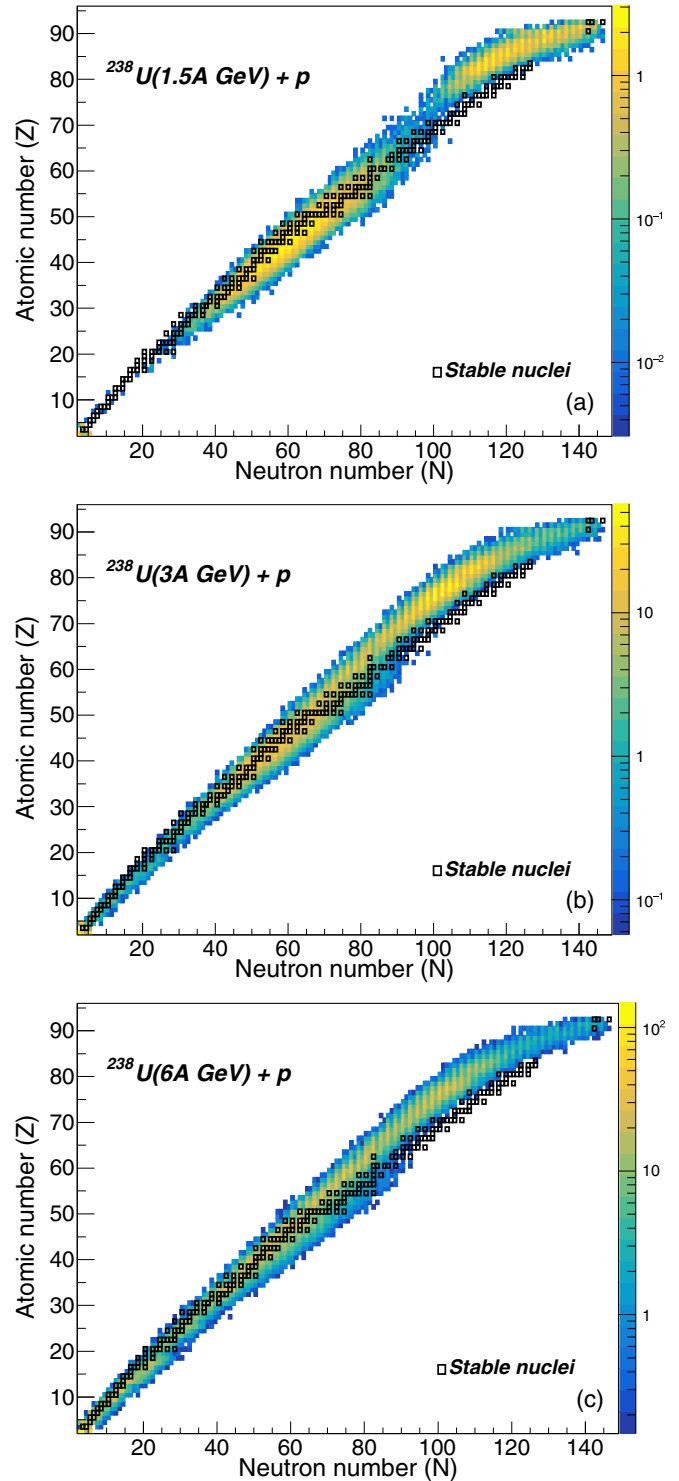


FIG. 12. Two-dimensional cluster plot of the isotopic production cross sections of  $\Lambda$  hypernuclei in  $\mu\text{b}$  shown as a chart of nuclides for proton-induced reactions on  $^{238}\text{U}$  at 1.5A GeV (a), 3.0A GeV (b), and 6.0A GeV (c). Open squares correspond to normal stable nuclei.

a function of the projectile kinetic energy for both nuclear systems. The same calculations for hypernuclei (dashed lines) also result in a reasonable description of the measured hyper-fission cross sections. We would like to remark here that in

both cases we only have one experimental data point and, thus, more measurements have to be performed to complete the evolution of the hyperfission cross sections with the projectile kinetic energy.

This new version of ABLA also allows for investigating other observables such as the mass distribution of hypernuclei produced in spallation reactions. This observable is shown in Fig. 11 for projectile kinetic energies of 1.5A [Fig. 11(a)], 3A [Fig. 11(b)], and 6A [Fig. 11(c)] GeV. At energies of 1.5A GeV, the more important decay processes are clearly the evaporation of light particles and hyperfission, while higher kinetic energies open the possibility of multifragmentation processes.

Finally, in Fig. 12 we display the isotope composition of hypernuclei produced by evaporation, multifragmentation, and fission processes on  $^{238}\text{U}$  at the same projectile kinetic energies indicated in Fig. 11. The production of hypernuclei is represented as a function of the proton and neutron number of each hyperfragment because this allows us for the overview and selection of what reaction and energy will be better for studying a specific hypernuclei. For instance, at kinetic energies of 1.5A GeV, Fig. 12(a), one could produce heavy neutron-deficient hypernuclei ( $70 < Z < 89$ ) close to the proton drip line through spallation reactions and neutron-rich hypernuclei ( $25 < Z < 60$ ) through fission reactions. Simultaneously, we could produce a lot of hypernuclei around the valley of stability. This would be the expected hypernuclei production at the future GSI-FAIR facility. Higher energies could also help to produce more neutron-deficient hypernuclear systems in the region of medium-mass and heavy hypernuclei ( $50 < Z < 89$ ) as shown in Figs. 12(b) and 12(c).

#### IV. CONCLUSIONS

The deexcitation model ABLA originally written in FORTRAN has been translated to C++ and extended to the strangeness sector, including the binding energies of  $\Lambda$  particles and its propagation through decay processes such as particle evaporation, multifragmentation, and fission. This improvement opens the possibility of investigating the formation of cold light, intermediate-mass, and heavy hypernuclei far from the stability region of normal nuclei. In particular, we have studied in this work the production of  $\Lambda$  hypernuclei in spallation reactions by coupling the deexcitation model ABLA to the version 6.0 of the Liège intranuclear cascade model INCL, which has also been extended recently to the strangeness sector.

The binding energies of  $\Lambda$  particles have been implemented in ABLA by including a parametrization of experimental data obtained from strangeness-exchanging ( $\pi^+$ ,  $K^+$ ) reactions. Then the propagation of the  $\Lambda$  particle through the

possible decay processes, such as particle evaporation, multifragmentation, and fission, is described according to statistical assumptions considering that the  $\Lambda$  particle acts inside the nucleus as a neutron. In fact, this is a good approximation since the  $\Lambda$  particle interaction within nuclear matter is of the same order as the nucleon one. We clearly demonstrate that hypernuclei can be produced in evaporation, multifragmentation, and fission processes similar to normal nuclei. Our calculations are able to describe the cross sections of hypernuclei produced in single strangeness-exchanging ( $\pi^+$ ,  $K^+$ ) reactions covering a large range of target nuclei. In addition, these calculations also provide a reasonable description of hyperfission processes of heavy nuclei, such as bismuth and uranium, which are clearly responsible for the production of very neutron-rich and neutron deficient medium-mass hypernuclei being more relevant at projectile kinetic energies between 1.5A and 3A GeV. At higher energies, the dominant decay channels for the production of hypernuclei are the multifragmentation and evaporation processes.

Finally, the ABLA model has also been implemented in the GEANT4 software package [54] for the simulation of future experiments aiming at the investigation of very neutron-rich and neutron-deficient hypernuclei with relativistic radioactive ion beams at worldwide nuclear physics facilities. Such state-of-the-art experiments may, thus, provide for the first time information on the isospin dependence of binding energies and decay lifetimes of hyperons in exotic nuclear matter, as well as the variation of fission-barrier heights in the presence of strange particles. These investigations would be carried out using state-of-the-art time projection chambers (TPC) like the one developed for the SAMURAI spectrometer at the RIKEN facility [165], which allows for the tracking of many charged particles and fragments simultaneously inside an intense magnetic field. Since for these studies one needs exotic beams at high kinetic energies ( $\gtrsim 1.5\text{A GeV}$ ), the best place to perform these experiments is the future FAIR facility [35] at Darmstadt (Germany), inserting, for instance, a TPC detector inside the large superconducting magnet GLAD [166]. In addition, neutron multiplicities would be measured with the highly segmented NeuLAND detector [167], allowing for complete kinematics measurements of all the reaction products.

#### ACKNOWLEDGMENTS

We wish to thank Dr. Alain Boudard and Dr. Davide Mancusi for enlightening discussions and Dr. Georg Schnabel for his technical support. This work has been partially supported by the EU ENSAR2 FP7 project (Grant Agreement No. 654002). J.L.R.-S. is thankful for the support by the Department of Education, Culture, and University Organization of the Regional Government of Galicia under the Postdoctoral Fellowship Grant No. ED481D-2021-018.

[1] M. Danysz and J. Pniewski, *Philos. Mag. Ser. A*, **44**, 348 (1953).  
 [2] H. Lenske, M. Dhar, T. Gaitanos, and X. Cao, *Prog. Part. Nucl. Phys.* **98**, 119 (2018).

[3] H. Park, H. Bhang, M. Youn, O. Hashimoto, K. Maeda, Y. Sato, T. Takahashi, K. Aoki, Y. D. Kim, H. Noumi, K. Omata, H. Ota, M. Sekimoto, T. Shibata, T. Hasegawa, H. Hotchi, Y.

- Ohta, S. Ajimura, and T. Kishimoto, *Phys. Rev. C* **61**, 054004 (2000).
- [4] D. J. Millener, C. B. Dover, and A. Gal, *Phys. Rev. C* **38**, 2700 (1988).
- [5] P. M. M. Maessen, T. A. Rijken, and J. J. de Swart, *Phys. Rev. C* **40**, 2226 (1989).
- [6] K. Tominaga, T. Ueda, M. Yamaguchi, N. Kijima, D. Okamoto, K. Miyagawa, and T. Yamada, *Nucl. Phys. A* **642**, 483 (1998).
- [7] J. Cugnon, A. Lejeune, and H.-J. Schulze, *Phys. Rev. C* **62**, 064308 (2000).
- [8] H.-J. Schulze, *Nucl. Phys. A* **835**, 19 (2010).
- [9] E. Hiyama and K. Nakazawa, *Annu. Rev. Nucl. Part. Sci.* **68**, 131 (2018).
- [10] J. Haidenbauer, *Phys. Rev. C* **102**, 034001 (2020).
- [11] I. Vidaña, A. Polls, A. Ramos, L. Engvik, and M. Hjorth-Jensen, *Phys. Rev. C* **62**, 035801 (2000).
- [12] H.-J. Schulze and T. Rijken, *Phys. Rev. C* **84**, 035801 (2011).
- [13] P. F. Bedaque and A. W. Steiner, *Phys. Rev. C* **92**, 025803 (2015).
- [14] R. Wirth and R. Roth, *Phys. Rev. Lett.* **117**, 182501 (2016).
- [15] M. Fortin, S. S. Avancini, C. Providência, and I. Vidaña, *Phys. Rev. C* **95**, 065803 (2017).
- [16] A. Gal, E. V. Hungerford, and D. J. Millener, *Rev. Mod. Phys.* **88**, 035004 (2016).
- [17] M. Danyasz, K. Garbowska, J. Pniewski, T. Pniewski, J. Zakrzewski, E. R. Fletcher, J. Lemonne, P. Renard, J. Sacton, W. T. Toner *et al.*, *Nucl. Phys.* **49**, 121 (1963).
- [18] H. Bando, T. Motoba, and J. Zofka, *Int. J. Mod. Phys. A* **5**, 4021 (1990), and references therein.
- [19] H. Shen and H. Toki, *Phys. Rev. C* **71**, 065208 (2005).
- [20] N. Kaiser, *Phys. Rev. C* **71**, 068201 (2005).
- [21] J. Haidenbauer, S. Petschauer, N. Kaiser, U.-G. Meissner, A. Nogga, and W. Weise, *Nucl. Phys. A* **915**, 24 (2013).
- [22] C. B. Dover, D. J. Millener, and A. Gal, *Phys. Rep.* **184**, 1 (1989).
- [23] L. Yordanova and V. Vasendina, *J. Phys.: Conf. Ser.* **503**, 012041 (2014).
- [24] M. Kapishin (BM@N Collaboration), *Nucl. Phys. A* **982**, 967 (2019).
- [25] J. Adam, L. Adamczyk, J. R. Adams, J. K. Adkins, G. Agakishiev, M. M. Aggarwal, Z. Ahammed, N. N. Ajitanand, I. Alekseev, D. M. Anderson *et al.* (STAR Collaboration), *Phys. Rev. C* **98**, 014910 (2018).
- [26] J. Adam, L. Adamczyk, J. R. Adams, J. K. Adkins, G. Agakishiev, M. M. Aggarwal, Z. Ahammed, I. Alekseev, D. M. Anderson, A. Aparin *et al.* (STAR Collaboration), *Nat. Phys.* **16**, 409 (2020).
- [27] B. Dönigus *et al.* (ALICE Collaboration), *Nucl. Phys. A* **904**, 547c (2013).
- [28] B. Dönigus *et al.* (ALICE Collaboration), *Eur. Phys. J. Web Conf.* **97**, 00013 (2015).
- [29] J. Messchendorp (PANDA Collaboration), *JPS Conf. Proc.* **13**, 010016 (2017).
- [30] K. Schönning, Hyperon and hypernuclear physics with PANDA at FAIR, in *Recent Progress in Few-Body Physics*, edited by N. Orr, M. Płoszajczak, F. Marqués, and J. Carbonell, Springer Proceedings in Physics, Vol. 238 (Springer, Cham, 2020), pp. 931–935.
- [31] I. Vassiliev, P. Senger, I. Kisel, and M. Zyzak (CBM Collaboration), *JPS Conf. Proc.* **17**, 092001 (2017).
- [32] C. Rappold and J. Lopez-Fidalgo, *Phys. Rev. C* **94**, 044616 (2016).
- [33] Y. L. Sun, A. S. Botvina, A. Obertelli, A. Corsi, and M. Bleicher, *Phys. Rev. C* **98**, 024903 (2018).
- [34] J. L. Rodríguez-Sánchez, J. C. David, J. Hirtz, A. Kelić-Heil, T. R. Saito, C. Scheidenberger *et al.*, *JPS Conf. Proc.* **32**, 010086 (2020).
- [35] <http://www.fair.de>.
- [36] L. N. Sheng *et al.*, *Nucl. Instrum. Methods Phys. Res., Sect. B* **469**, 1 (2020).
- [37] T. R. Saito, H. Ekawa, and M. Nakagawa, *Eur. Phys. J. A* **57**, 159 (2021).
- [38] T. R. Saito *et al.* (HypHI Collaboration), *Nucl. Phys. A* **881**, 218 (2012).
- [39] P. Danielewicz, R. Lacey, and W. G. Lynch, *Science* **298**, 1592 (2002).
- [40] J. R. Torres, F. Gulminelli, and D. P. Menezes, *Phys. Rev. C* **95**, 025201 (2017).
- [41] R. Serber, *Phys. Rev.* **72**, 1114 (1947).
- [42] J. Cugnon, C. Volant, and S. Vuillier, *Nucl. Phys. A* **620**, 475 (1997).
- [43] A. Boudard, J. Cugnon, S. Leray, and C. Volant, *Phys. Rev. C* **66**, 044615 (2002).
- [44] D. Mancusi, R. J. Charity, and J. Cugnon, *Phys. Rev. C* **82**, 044610 (2010).
- [45] S. Pedoux, J. Cugnon, A. Boudard, J.-C. David, and S. Leray, *Adv. Space Res.* **44**, 926 (2009).
- [46] D. Mancusi, S. Lo Meo, N. Colonna, A. Boudard, M. A. Cortés-Giraldo, J. Cugnon, J.-C. David, S. Leray, J. Lerendegui-Marco, C. Massimi, and V. Vlachoudis, *Eur. Phys. J. A* **53**, 80 (2017).
- [47] J.-C. David, A. Boudard, J. Cugnon, J. Hirtz, S. Leray, D. Mancusi, and J. L. Rodríguez-Sánchez, *Eur. Phys. J. Plus* **133**, 253 (2018).
- [48] J. Hirtz, J.-C. David, A. Boudard, J. Cugnon, S. Leray, and D. Mancusi, *Eur. Phys. J. Plus* **133**, 436 (2018).
- [49] J. L. Rodríguez-Sánchez, J. C. David, J. Hirtz, J. Cugnon, and S. Leray, *Phys. Rev. C* **98**, 021602(R) (2018).
- [50] J. Hirtz, J.-C. David, A. Boudard, J. Cugnon, S. Leray, I. Leya, J. L. Rodríguez-Sánchez, and G. Schnabel, *Phys. Rev. C* **101**, 014608 (2020).
- [51] A. S. Botvina *et al.*, *Nucl. Phys. A* **584**, 737 (1995).
- [52] P. N. Peplowski, *Nucl. Phys. A* **1006**, 122067 (2021).
- [53] J.-C. David, *Eur. Phys. J. A* **51**, 68 (2015).
- [54] J. Allison *et al.*, *Nucl. Inst. Meths. Phys. Res. A* **835**, 186 (2016).
- [55] R. J. Charity *et al.*, *Nucl. Phys. A* **483**, 371 (1988).
- [56] D. P. Bondorf, A. S. Botvina *et al.*, *Phys. Rep.* **257**, 133 (1995).
- [57] A. Kelić, M. V. Ricciardi, and K.-H. Schmidt, in *Proceedings of Joint ICTP-IAEA Advanced Workshop on Model Codes for Spallation Reactions, ICTP Trieste, Italy, 4–8 February 2008*, edited by D. Filges, S. Leray, Y. Yariv, A. Mengoni, A. Stanculescu, and G. Mank (IAEA INDC, Vienna, 2008), pp. 181–221.
- [58] S. Leray, J.-C. David, M. Khandaker, G. Mank, A. Mengoni, N. Otsuka, D. Filges, F. Gallmeier, A. Konobeyev, and R. Michel, *J. Korean Phys. Soc.* **59**, 791 (2011); IAEA Benchmark of Spallation Models, <http://www-nds.iaea.org/spallations>.
- [59] Y. Yariv and Z. Fraenkel, *Phys. Rev. C* **20**, 2227 (1979).

- [60] J. Cugnon, *Phys. Rev. C* **23**, 2094 (1981).
- [61] K. K. Gudima, S. G. Mashnik, and V. D. Toneev, *Nucl. Phys. A* **401**, 329 (1983).
- [62] K. Niita, S. Chiba, T. Maruyama, T. Maruyama, H. Takada, T. Fukahori, Y. Nakahara, and A. Iwamoto, *Phys. Rev. C* **52**, 2620 (1995).
- [63] H. Duarte, *Phys. Rev. C* **75**, 024611 (2007).
- [64] D. Mancusi, A. Boudard, J. Cugnon, J.-C. David, T. Gorbinet, and S. Leray, *Phys. Rev. C* **84**, 064615 (2011).
- [65] J.-C. David and I. Leya, *Prog. Part. Nucl. Phys.* **109**, 103711 (2019).
- [66] D. Mancusi, A. Boudard, J. Carbonell, J. Cugnon, J.-C. David, and S. Leray, *Phys. Rev. C* **91**, 034602 (2015).
- [67] D. Mancusi, A. Boudard, J. Cugnon, J.-C. David, P. Kaitaniemi, and S. Leray, *Phys. Rev. C* **90**, 054602 (2014).
- [68] A. Boudard, J. Cugnon, J.-C. David, S. Leray, and D. Mancusi, *Phys. Rev. C* **87**, 014606 (2013).
- [69] T. Aoust and J. Cugnon, *Phys. Rev. C* **74**, 064607 (2006).
- [70] H. D. Vries, C. W. D. Jager, and C. D. Vries, *At. Data Nucl. Data Tables* **36**, 495 (1987).
- [71] J. L. Rodríguez-Sánchez, J. C. David, D. Mancusi, A. Boudard, J. Cugnon, and S. Leray, *Phys. Rev. C* **96**, 054602 (2017).
- [72] J. Cugnon, D. L'Hôte, and J. Vandermeulen, *Nucl. Instrum. Methods Phys. Res., Sect. B* **111**, 215 (1996).
- [73] A. Ozawa, T. Suzuki, and I. Tanihata, *Nucl. Phys. A* **693**, 32 (2001).
- [74] M. Takechi, M. Fukuda, M. Mihara, K. Tanaka, T. Chinda, T. Matsumasa, M. Nishimoto, R. Matsumiya, Y. Nakashima, H. Matsubara, K. Matsuta, T. Minamisono, T. Ohtsubo, T. Izumikawa, S. Momota, T. Suzuki, T. Yamaguchi, R. Koyama, W. Shinozaki, M. Takahashi, A. Takizawa, T. Matsuyama, S. Nakajima, K. Kobayashi, M. Hosoi, T. Suda, M. Sasaki, S. Sato, M. Kanazawa, and A. Kitagawa, *Phys. Rev. C* **79**, 061601(R) (2009).
- [75] K. Tanida, H. Tamura, D. Abe, H. Akikawa, K. Araki, H. Bhang, T. Endo, Y. Fujii, T. Fukuda, O. Hashimoto, K. Imai, H. Hotchi, Y. Kakiguchi, J. H. Kim, Y. D. Kim, T. Miyoshi, T. Murakami, T. Nagae, H. Noumi, H. Outa, K. Ozawa, T. Saito, J. Sasao, Y. Sato, S. Satoh, R. I. Sawafuta, M. Sekimoto, T. Takahashi, L. Tang, H. H. Xia, S. H. Zhou, and L. H. Zhu, *Phys. Rev. Lett.* **86**, 1982 (2001).
- [76] P. Chomaz, M. Colonna, and J. Randrup, *Phys. Rep.* **389**, 263 (2004).
- [77] K.-H. Schmidt, M. V. Ricciardi, A. S. Botvina, and T. Enqvist, *Nucl. Phys. A* **710**, 157 (2002).
- [78] J. B. Natowitz, R. Wada, K. Hagel, T. Keutgen, M. Murray, A. Makeev, L. Qin, P. Smith, and C. Hamilton, *Phys. Rev. C* **65**, 034618 (2002).
- [79] C. Sienti *et al.*, *Nucl. Phys. A* **787**, 627 (2007).
- [80] A. S. Botvina, N. Buyukcizmeci, M. Erdogan, J. Lukasik, I. N. Mishustin, R. Ogul, and W. Trautmann, *Phys. Rev. C* **74**, 044609 (2006).
- [81] A. S. Botvina *et al.*, *Nucl. Phys. A* **475**, 663 (1987).
- [82] V. F. Weisskopf and D. H. Ewing, *Phys. Rev.* **57**, 472 (1940).
- [83] W. J. Huang, G. Audi, M. Wang, F. G. Kondev, S. Naimi, and X. Xu, *Chin. Phys. C* **41**, 030002 (2017).
- [84] W. W. Qu *et al.*, *Nucl. Phys. A* **868**, 1 (2011).
- [85] R. Bass, in *Proceedings of the Symposium on Deep-Inelastic and Fusion Reactions with Heavy Ions* (Springer Verlag, Berlin, 1980).
- [86] C. Samanta, P. Roy Chowdhury, and D. N. Basu, *J. Phys. G.: Nucl. Part. Phys.* **32**, 363 (2006).
- [87] A. S. Botvina, N. Buyukcizmeci, A. Ergun, R. Ogul, M. Bleicher, and J. Pochodzalla, *Phys. Rev. C* **94**, 054615 (2016).
- [88] J. N. Hu, A. Li, H. Shen, and H. Toki, *Prog. Theor. Exp. Phys.* **2014**, 013D02 (2014).
- [89] S. Hilarej and S. Goriely, *Nucl. Phys. A* **779**, 63 (2006).
- [90] B. Nerlo-Pomorska and K. Pomorski, *Int. J. Mod. Phys. E* **15**, 471 (2006).
- [91] B. Krusche and K. P. Lieb, *Phys. Rev. C* **34**, 2103 (1986).
- [92] A. Gilbert and A. G. W. Cameron, *Can. J. Phys.* **43**, 1446 (1965).
- [93] H. A. Bethe, *Rev. Mod. Phys.* **9**, 69 (1937).
- [94] A. V. Ignatyuk, K. K. Istekov, and G. N. Smirenkin, *Yad. Fiz.* **29**, 875 (1979) [*Sov. J. Nucl. Phys.* **29**, 450 (1979)].
- [95] P. Möller, J. R. Nix, W. D. Myers, and W. J. Swiatecki, *At. Nucl. Data Tables* **59**, 185 (1995).
- [96] J. R. Huizenga and L. G. Moretto, *Annu. Rev. Nucl. Part. Sci.* **22**, 427 (1972).
- [97] T. von Egidy, H. H. Schmidt, and A. N. Behkami, *Nucl. Phys. A* **481**, 189 (1988).
- [98] A. V. Ignatyuk *et al.*, *Yad. Fiz.* **21**, 485 (1975) [*Sov. J. Nucl. Phys.* **21**, 255 (1975)].
- [99] J. Töke and W. J. Swiatecki, *Nucl. Phys. A* **372**, 141 (1981).
- [100] A. V. Ignatyuk, M. G. Itkis, V. N. Okolovich, G. N. Smirenkin, and A. S. Tishin, *Yad. Fiz.* **21**, 1185 (1975) [*Sov. J. Nucl. Phys.* **21**, 612 (1975)].
- [101] W. D. Myers and W. J. Swiatecki, *Ann. Phys. (NY)* **84**, 186 (1974).
- [102] W. D. Myers and W. J. Swiatecki, *Nucl. Phys. A* **601**, 141 (1996).
- [103] A. V. Karpov, A. Kelić, and K.-H. Schmidt, *J. Phys. G* **35**, 035104 (2008).
- [104] K.-H. Schmidt *et al.*, *Z. Phys. A* **308**, 215 (1982).
- [105] A. V. Ignatyuk, M. G. Itkis, V. N. Okolovich, and G. R. Ruskina, *Yad. Fiz.* **25**, 25 (1977) [*Sov. J. Nucl. Phys.* **25**, 13 (1977)].
- [106] A. V. Ignatyuk, in *Proceedings on the Conference Bologna 2000: Structure of the Nucleus at the Dawn of the Century*, edited by G. C. Bonsignori, M. Bruno, A. Ventura, and D. Vretenar (World Scientific, Singapore, 2001).
- [107] S. Bjornholm *et al.*, in *Proceedings of the Third IAEA Symposium on the Physics, Chemistry of Fission, Rochester, NY, 13–17 August 1973*, Vol. 1 (IAEA, Vienna, 1974), p. 367.
- [108] J. R. Huizenga *et al.*, *Nucl. Phys. A* **223**, 589 (1974).
- [109] A. R. Junghans *et al.*, *Nucl. Phys. A* **629**, 635 (1998).
- [110] R. W. Hasse and W. D. Myers, *Geometrical Relationships of Macroscopic Nuclear Physics* (Springer-Verlag, Berlin, 1988).
- [111] S. Cohen and W. J. Swiatecki, *Ann. Phys.* **22**, 406 (1963).
- [112] M. V. Ricciardi *et al.*, *Nucl. Phys. A* **733**, 299 (2004).
- [113] P. Axel, *Phys. Rev.* **126**, 671 (1962).
- [114] N. Bohr and J. A. Wheeler, *Phys. Rev.* **56**, 426 (1939).
- [115] L. G. Moretto, *Nucl. Phys. A* **247**, 211 (1975).
- [116] A. J. Sierk, *Phys. Rev. C* **33**, 2039 (1986).
- [117] H. A. Kramers, *Phys. (Amsterdam, Neth.)* **7**, 284 (1940).
- [118] J. R. Nix, *Ann. Phys.* **41**, 52 (1967).
- [119] H. Risiken, *The Fokker-Planck Equation* (Springer-Verlag, Berlin, 1989).
- [120] B. Jurado, K.-H. Schmidt, and J. Benlliure, *Phys. Lett. B* **553**, 186 (2003).

- [121] B. Jurado, C. Schmitt, K.-H. Schmidt, J. Benlliure, and A. R. Junghans, *Nucl. Phys. A* **747**, 14 (2005).
- [122] C. Schmitt, K.-H. Schmidt, A. Kelić, A. Heinz, B. Jurado, and P. N. Nadtochy, *Phys. Rev. C* **81**, 064602 (2010).
- [123] S. Chandrasekhar, *Rev. Mod. Phys.* **15**, 1 (1943).
- [124] Y. Ayyad, J. Benlliure, J. L. Rodríguez-Sánchez, A. Bacquias, A. Boudard, E. Casarejos, T. Enqvist, M. Fernandez, V. Henzl, V. Henzlova, B. Jurado, A. Kelic-Heil, T. Kurtukian, S. Lukic, P. Nadtochy, D. Perez-Loureiro, R. Pleskac, F. Farget, M. V. Ricciardi, K. H. Schmidt, C. Schmitt, and S. N. Ngoc, *Phys. Rev. C* **91**, 034601 (2015).
- [125] J. L. Rodríguez-Sánchez *et al.*, *Phys. Rev. C* **91**, 064616 (2015); **92**, 044612 (2015).
- [126] J. L. Rodríguez-Sánchez *et al.*, *Phys. Rev. C* **90**, 064606 (2014).
- [127] A. Gavron *et al.*, *Phys. Rev. C* **13**, 2374 (1976).
- [128] V. M. Strutinsky and S. Bjørnholm, in *Proceedings of the International Symposium on Nuclear Structure, 4–11 July 1968, Dubna* (IAEA, Vienna, 1968).
- [129] S. Bjørnholm and J. E. Lynn, *Rev. Mod. Phys.* **52**, 725 (1980).
- [130] N. Buyukcizmeci, A. S. Botvina, A. Ergun, R. Ogul, and M. Bleicher, *Phys. Rev. C* **98**, 064603 (2018).
- [131] D. B. Ion, M. Ivaşcu, and R. Ion-Mihai, *Rev. Roum. Phys.* **34**, 461 (1989).
- [132] F. Minato, S. Chiba, and K. Hagino, *Nucl. Phys. A* **831**, 150 (2009).
- [133] K.-H. Schmidt, A. Kelić, and M. V. Ricciardi, *EPL* **83**, 32001 (2008).
- [134] J. Benlliure, A. Grewe, M. de Jong, K.-H. Schmidt, and S. Zhdanov, *Nucl. Phys. A* **628**, 458 (1998).
- [135] K. Kruglov, A. Andreyev, B. Bruyneel *et al.*, *Eur. Phys. J. A* **14**, 365 (2002).
- [136] A. Ya. Rusanov, M. G. Itkis, and V. N. Okolovic, *Phys. At. Nucl.* **60**, 683 (1997).
- [137] P. N. Nadtochy, G. D. Adeev, and A. V. Karpov, *Phys. Rev. C* **65**, 064615 (2002).
- [138] P. Armbruster, *Nucl. Phys. A* **140**, 385 (1970).
- [139] J. L. Rodríguez-Sánchez *et al.*, *Phys. Rev. C* **94**, 061601(R) (2016).
- [140] U. Brosa, S. Grossmann, and A. Müller, *Phys. Rep.* **197**, 167 (1990).
- [141] M. G. Itkis, V. N. Okolovich, A. Y. Rusanov, and G. N. Smirenkin, *Sov. J. Part. Nucl.* **19**, 301 (1988).
- [142] B. D. Wilkins, E. P. Steinberg, and R. R. Chasman, *Phys. Rev. C* **14**, 1832 (1976).
- [143] C. Böckstiegel, S. Steinhäuser, K.-H. Schmidt, H. G. Clerc, A. Grewe, A. Heinz, M. de Jong, A. R. Junghans, J. Müller, and B. Voss, *Nucl. Phys. A* **802**, 12 (2008).
- [144] T. A. Armstrong, J. P. Bocquet, G. Ericsson, T. Johansson, T. Krogulski, R. A. Lewis, F. Malek, M. Maurel, E. Monnard, J. Mougey, H. Nifenecker, J. Passaneau, P. Perrin, S. M. Polikanov, M. Rey-Campagnolle, C. Ristori, G. A. Smith, and G. Tibell, *Phys. Rev. C* **47**, 1957 (1993).
- [145] J. P. Bocquet *et al.*, *Phys. Lett. B* **182**, 146 (1986).
- [146] H. Nifenecker and F. Malek, *Nucl. Phys. A* **531**, 539 (1991).
- [147] M. V. Ricciardi, P. Armbruster, J. Benlliure, M. Bernas, A. Boudard, S. Czajkowski, T. Enqvist, A. Kelic, S. Leray, R. Legrain, B. Mustapha, J. Pereira, F. Rejmund, K. H. Schmidt, C. Stephan, L. Tassan-Got, C. Volant, and O. Yordanov, *Phys. Rev. C* **73**, 014607 (2006).
- [148] C. Villagrasa-Canton, A. Boudard, J. E. Ducret, B. Fernandez, S. Leray, C. Volant, P. Armbruster, T. Enqvist, F. Hammache, K. Helariutta, B. Jurado, M. V. Ricciardi, K. H. Schmidt, K. Summerer, F. Vives, O. Yordanov, L. Audouin, C. O. Bacri, L. Ferrant, P. Napolitani, F. Rejmund, C. Stephan, L. Tassan-Got, J. Benlliure, E. Casarejos, M. Fernandez-Ordonez, J. Pereira, S. Czajkowski, D. Karamanis, M. Pravikoff, J. S. George, R. A. Mewaldt, N. Yanasak, M. Wiedenbeck, J. J. Connell, T. Faestermann, A. Heinz, and A. Junghans, *Phys. Rev. C* **75**, 044603 (2007).
- [149] J. Alcantara-Nunez, J. Benlliure, C. Paradela, C. Perez-Loureiro, J. L. Rodriguez-Sanchez, L. Audouin, A. Boudard, E. Casarejos, T. Enqvist, F. Farget, M. Fernandez-Ordonez, A. Heinz, V. Henzl, D. Henzlova, A. Kelic-Heil, A. Lafriashk, S. Leray, P. Napolitani, J. Pereira, M. V. Ricciardi, C. Stephan, K. H. Schmidt, C. Schmitt, L. Tassan-Got, C. Villagrasa, C. Volant, O. Yordanov, *Phys. Rev. C* **92**, 024607 (2015).
- [150] C. Paradela, L. Tassan-Got, J. Benlliure, J. L. Rodríguez-Sánchez, L. Audouin, A. Boudard, E. Casarejos, T. Enqvist, J. E. Ducret, F. Farget, B. Fernandez-Dominguez, M. Fernandez-Ordonez, L. Giot, A. Heinz, V. Henzl, D. Henzlova, A. Kelic-Heil, A. Lafriashk, S. Leray, P. Napolitani, J. Pereira, D. Perez-Loureiro, M. V. Ricciardi, C. Stephan, K. H. Schmidt, C. Schmitt, C. Villagrasa, C. Volant, and O. Yordanov, *Phys. Rev. C* **95**, 044606 (2017).
- [151] J. Benlliure and J. L. Rodríguez-Sánchez, *Eur. Phys. J. Plus* **132**, 120 (2017).
- [152] M. Fidelus, D. Filges, F. Goldenbaum, H. Hodde, A. Jany, L. Jarczyk, B. Kamys, M. Kistryn, S. Kistryn, S. Kliczewski, E. Kozik, P. Kulesa, H. Machner, A. Magiera, B. Piskorn-Ignatowicz, K. Pysz, Z. Rudy, S. K. Sharma, R. Siudak, and M. Wojciechowski, *Phys. Rev. C* **89**, 054617 (2014).
- [153] Y. Ayyad, J. Benlliure, E. Casarejos, H. Alvarez-Pol, A. Bacquias, A. Boudard, M. Caamano, T. Enqvist, V. Fohr, A. Kelic-Heil, K. Kezzar, S. Leray, D. Mancusi, C. Paradela, D. Perez-Loureiro, R. Pleskac, J. L. Rodriguez-Sanchez, and D. Tarrío, *Phys. Rev. C* **89**, 054610 (2014).
- [154] S. Lo Meo, D. Mancusi, C. Massimi, G. Vannini, and A. Ventura, *Nucl. Phys. A* **933**, 43 (2015).
- [155] P. Napolitani, K. Schmidt, L. Tassan-Got, P. Armbruster, T. Enqvist, A. Heinz, V. Henzl, D. Henzlova, A. Kelic, R. Pleskac, M. V. Ricciardi, C. Schmitt, O. Yordanov, L. Audouin, M. Bernas, A. Lafriashk, F. Rejmund, C. Stephan, J. Benlliure, E. Casarejos, M. Fernandez Ordonez, J. Pereira, A. Boudard, B. Fernandez, S. Leray, C. Villagrasa, and C. Volant, *Phys. Rev. C* **76**, 064609 (2007).
- [156] T. Enqvist *et al.*, *Nucl. Phys. A* **686**, 481 (2001).
- [157] A. Kelić, K. H. Schmidt, T. Enqvist, A. Boudard, P. Armbruster, J. Benlliure, M. Bernas, S. Czajkowski, R. Legrain, S. Leray, B. Mustapha, M. Pravikoff, F. Rejmund, C. Stephan, J. Taieb, L. Tassan-Got, C. Volant, and W. Wlazlo, *Phys. Rev. C* **70**, 064608 (2004).
- [158] P. Armbruster, J. Benlliure, M. Bernas, A. Boudard, E. Casarejos, S. Czajkowski, T. Enqvist, S. Leray, P. Napolitani, J. Pereira, F. Rejmund, M. V. Ricciardi, K. H. Schmidt, C. Stephan, J. Taieb, L. Tassan-Got, and C. Volant, *Phys. Rev. Lett.* **93**, 212701 (2004).
- [159] T. Hasegawa, O. Hashimoto, S. Homma, T. Miyachi, T. Nagae, M. Sekimoto, T. Shibata, H. Sakaguchi, T. Takahashi, K. Aoki, H. Noumi, H. Bhang, M. Youn, Y. Gavrilov, S. Ajimura,

- T. Kishimoto, A. Ohkusu, K. Maeda, R. Sawafta, and R. P. Redwine, *Phys. Rev. C* **53**, 1210 (1996).
- [160] M. Akei *et al.*, *Nucl. Phys. A* **534**, 478 (1991).
- [161] P. H. Pile, S. Bart, R. E. Chrien, D. J. Millener, R. J. Sutter, N. Tsoupas, J. C. Peng, C. S. Mishra, E. V. Hungerford, T. Kishimoto, L. G. Tang, W. vonWitsch, Z. Xu, K. Maeda, D. Gill, R. McCrady, B. Quinn, J. Seydoux, J. W. Sleight, R. L. Stearns, H. Plendl, A. Rafatian, and J. Reidy, *Phys. Rev. Lett.* **66**, 2585 (1991).
- [162] IAEA EXFOR database, <https://www-nds.iaea.org/exfor/exfor.htm>.
- [163] H. Ohm, T. Hermes, W. Borgs, H. R. Koch, R. Maier, D. Prasuhn, H. J. Stein, O. W. B. Schult, K. Pysz, Z. Rudy, L. Jarczyk, B. Kamys, P. Kulesa, A. Strzalkowski, W. Cassing, Y. Uozumi, and I. Zychor, *Phys. Rev. C* **55**, 3062 (1997).
- [164] P. Kulesa *et al.*, *Phys. Lett. B* **427**, 403 (1998).
- [165] G. Jhang *et al.*, *Phys. Lett. B* **813**, 136016 (2021).
- [166] B. Gastineau *et al.*, *Trans. App. Supercond.* **18**, 407 (2008).
- [167] K. Boretzky *et al.*, *Nucl. Instrum. Methods Phys. Res. A* **1014**, 165701 (2021).